Site C0017[1]

Expedition 331 Scientists[2]

Chapter contents

Background and objectives 1
Operations 1
Lithostratigraphy 2
Biostratigraphy 4
Petrology 4
Geochemistry 5
Microbiology 6
Physical properties 8
References 10
Figures 12
Tables 39

Background and objectives

Integrated Ocean Drilling Program (IODP) Site C0017 is located 1.6 km east of the hydrothermal vent sites in the central valley of Iheya North Knoll (see Fig. F3 in Expedition 331 Scientists, 2011a). Based on the multichannel seismic (MCS) survey (see Figs. F5 and F6 in Expedition 331 Scientists, 2011a), the uppermost 100 meters below seafloor (mbsf) probably consists of hemipelagic sediment. At ~100 mbsf, a strong seismic reflection is continuous from the hydrothermal vent sites at Site C0016 eastward through Sites C0013 and C0014. This reflection represents a potential interface between hemipelagic sediments and pyroclastic flow deposits. Below this reflection the subseafloor structure becomes obscure. Potential volcanic basement, however, may be identifiable at ~450 mbsf at Site C0017.

Heat flow measured in the sediments near Site C0017 is quite low (see Fig. F2 in Expedition 331 Scientists, 2011c). The surficial thermal gradient is one order of magnitude lower than the average thermal gradient of the nonhydrothermal, trough-filling sediments in the middle Okinawa Trough. This low heat flow anomaly strongly suggests that Site C0017 is located within a large-scale local recharge zone. Heat flow data also indicate that there are areas with relatively high thermal gradients several hundreds of meters from Site C0017, suggesting that the local recharge/discharge boundary of the Iheya North hydrothermal system may be quite narrow in the east–west direction in the vicinity of Site C0017.

The scientific objectives for Site C0017 are to understand the potential discharge and recharge dynamics around the central valley of Iheya North Knoll and to clarify the interaction between subseafloor physical-chemical variations and microbial community structures and functions.

Operations

Arrival at Site C0017

The D/V *Chikyu* moved to Site C0017 and began coring on the night between 26 and 27 September 2010 (Fig. F1; Table T1). The plan was to core as deep as possible in the 2–3 days available.

[1]Expedition 331 Scientists, 2011. Site C0017. *In* Takai, K., Mottl, M.J., Nielsen, S.H., and the Expedition 331 Scientists, *Proc. IODP,* 331: Tokyo (Integrated Ocean Drilling Program Management International, Inc.). doi:10.2204/iodp.proc.331.107.2011
[2]Expedition 331 Scientists' addresses.

doi:10.2204/iodp.proc.331.107.2011

Hole C0017A

After tagging the seafloor on 27 September 2010 at 1154.5 m drilling depth below seafloor (DSF), Hole C0017A was spudded with the hydraulic piston coring system (HPCS), retrieving mudline and penetrating to 8.8 mbsf. The bit pulled out of hole on core retrieval, ending Hole C0017A.

Hole C0017B

Hole C0017B was washed and drilled down to the penetration depth of Core 331-C0017A-1H on 27 September 2010 and then shot with the HPCS just 1 m south of Hole C0017A. Penetration and recovery were a perfect 9.5 m, but again the bit pulled out when we retrieved the core, ending Hole C0017B.

Hole C0017C

On 27 September 2010, the *Chikyu* offset ~8 m northeast to begin drilling deeper. Core 331-C0017C-1H was shot with the HPCS after washing and drilling down to the penetration depth of Core 331-C0017B-1H. Core 331-C0017C-2H was shot with the HPCS, penetrated fully, and recovered 8.5 m of sediment with a little overpull at the end. To avoid getting stuck in the formation, we switched to the extended shoe coring system (ESCS) for Core 331-C0017C-3X. However, upon retrieval of the core barrel we found the shoe and core catcher sub were missing and decided to abandon the hole. An HPCS inner barrel was run through the drill string after pulling out, to ascertain that nothing was left inside the pipe.

Hole C0017D

Hole C0017D was spudded on 27 September 2010, 5 m northeast of Hole C0017C. After washing and drilling down to 59.9 mbsf, skipping an interval of unrecoverable volcanic rubble, and recovering a failed ESCS coring attempt, Core 331-C0017D-1H was shot with the HPCS and recovered 9.5 m from a 9.2 m advance. Core 331-C0017D-2H was also shot with the HPCS, recovering 9 m from a 9.5 m advance. Core 331-C0017D-3H, however, recovered nothing from a 6.0 m advance, returning only a broken flapper and a cracked liner. Core 331-C0017D-4H likewise returned no sediment and had no advance, so we switched to the extended punch coring system (EPCS) to continue beyond 84.6 mbsf. With no recovery from a 9.5 m EPCS advance, we switched back to the ESCS, which returned 1.8 m from another advance of 9.5 m. As the formation seemed softer, we switched back to the HPCS and gained 100% recovery from an 8.5 m advance into sticky mud between 103.6 and 112.1 mbsf. Switching back to the EPCS returned only a few centimeters in the core catcher from a 9.5 m advance, so we went back to the ESCS. This change, surprisingly, gave us two good cores (331-C0017D-9X and 10X) with 107.8% and 68.4% recovery, respectively. However, during retrieval of Core 331-C0017D-11X, the sinker bar broke, leaving Core 11X in the hole at 149.6 mbsf. Fishing for Core 11X was unsuccessful because we did not have a tool onboard that would fit. The core was retrieved via a pipe trip, returning 4.8 m of core (50.5% of a 9.5 m advance) from a depth of 140.1–149.6 mbsf.

After pulling out, Hole C0017D was reentered unguided on the night of 28 September, and Core 331-C0017D-12H was taken on the morning of 29 September. This final shot penetrated 1 m to 150.6 mbsf but retrieved only a little gravel in the core catcher. The main reason for attempting the reentry and last core, however, was to get a temperature reading from either the advanced piston corer temperature tool (APCT3) shoe or one of the thermoseal strips taped to the inner barrel. The thermoseal strips returned a temperature measurement of 90° ± 5°C (three replicate strips), so Site C0017 ended very successfully at 150.6 mbsf with Core 331-C0017D-12H.

Lithostratigraphy

Site C0017 consists mainly of hemipelagic homogeneous mud, pumiceous sediment, and volcaniclastic-pumiceous mixed sand, without the obvious hydrothermal alteration seen at previous sites. Based on sediment character and structure, major mineral composition, and the occurrence of microfossils, sediments recovered from the four holes drilled (Holes C0017A, C0017B, C0017C, and C0017D) consist of three main sediment types: hemipelagic mud, coarse angular pumiceous gravel, and volcanic sands with erosional bases. These sediments and lithologies are similar to those of Unit I encountered at Sites C0014 and C0015. However, the unaltered sedimentary sequence drilled at Site C0017 is much more vertically extensive, and subdivision may be drawn on the basis of the relative predominance of hemipelagic mud or volcaniclastic sediments. This divides the stratigraphy at Site C0017 into four units (Fig. **F2;** Table **T2**). An upper unit (Unit I), dominantly composed of hemipelagic mud from 0 to 18.5 mbsf, is underlain by two units dominated by pumiceous gravel from 19.1 to 36.2 mbsf (Unit II) and 61.1 to 78.8 mbsf (Unit III). The interval from 36.1 to 61.1 mbsf was not cored, so it was not possible to group Unit II and Unit III as a single unit, despite the strong sedimentological similarity between them. Additionally, no core was recovered in the interval

from 78.8 to 94.3 mbsf. The deepest portion of the cored interval, from 94.3 to 144.7 mbsf (Unit IV) is dominated by hemipelagic mud. The thicknesses of individual beds of mud and gravel at Site C0017 are significantly greater than those at Site C0014, consistent with Site C0017's location on the downthrown side of a normal fault.

Sediment types at Site C0017

There is little apparent systematic vertical variation in sediment types at Site C0017. Unless stated otherwise, the following description of sediment types applies to all four lithostratigraphic units at the site.

Hemipelagic mud

Hemipelagic mud is the dominant sediment type in Unit I (0 to ~18.5 mbsf) and Unit IV (~94 to ~145 mbsf) but also occurs in Units II and III (Fig. F2). This mud is primarily composed of hemipelagic homogeneous silty clay or clayey silt, with widely distributed foraminifers and occasional lenticular pumiceous sand patches, gravels, and mud clasts. The grayish olive to dark olive-gray color and uniformity of the mud make it easy to recognize. Foraminifers are mostly fresh and intact and are only rarely reworked, reflecting an autochthonous source. They should be useful for postcruise research that aims to establish the late Quaternary chronostratigraphy in this area and to reconstruct paleoenvironments. The relatively uniform, homogeneous, and structureless mud in the upper 18.5 m of sediments in Holes C0017A and C0017B (Unit I) reflects a typical hemipelagic depositional environment.

In contrast, Unit IV (Cores 331-C0017D-6X, 7H, 9X, 10X, and 11X; ~94.3 to ~144.7 mbsf) comprises laminated and interbedded clay and silt and very fine sand, with homogeneous clay predominant. Layers of silt and very fine sand (1–5 cm thickness) commonly form upward-fining sequences and possess erosional bases that create sharp contacts with the underlying homogeneous dark gray clay (Fig. F3). From X-ray diffraction (XRD) analyses (Table T3), the mineralogy of these silty and fine sandy layers is dominated by probably locally derived volcanic glass, quartz, and feldspar. Along with calcite, muscovite, chlorite, and dolomite, they are also the main components of the overlying and underlying homogeneous clay. These coarser grained layers are probably formed primarily by volcanic eruption and episodic gravity flows related to volcanic and seismic activity.

Pumiceous gravel and lithoclast-rich horizons

The pumiceous gravel and lithoclast-rich horizons sediment type consists of poorly sorted pumiceous sediments dominated by coarse-grained angular woody pumiceous gravels (Fig. F4). It generally has a gradational contact with finer overlying pelagic or volcaniclastic sediments but mostly sharp contacts with the underlying sediments. Pumiceous gravels predominate in Unit II (19.1–36.2 mbsf) and Unit III (61.1–78.8 mbsf) but are also found within Units I and IV. This sediment type shares similar characteristics and major mineral compositions with pumiceous sediments encountered at Site C0014, and especially Site C0015.

The pumice encountered at Site C0017 can be divided into two types: one fresh and white-gray to greenish and the other oxidized and stained yellow to brown. It has similar appearance and bulk mineralogy to that found at Site C0014. Oxidized pumice is abundant between ~26 and 35 mbsf in Hole C0017C. Occasionally, the greenish pumice gravels and clasts (Fig. F3), which are inferred to contain glauconite (Weigland et al., 2003), are mixed with oxidized fragments, which are softer and more fragile than the fresh pumice and easily broken during visual examination. The significance of the oxidized pumice is discussed in more detail in **"Petrology."**

Volcaniclastic and pumiceous mixed sand

Gray to black, fine to coarse sand and gravels with a mixture of volcaniclastic and pumiceous components are irregularly distributed throughout all four units at C0017 (Fig. F2). A number of individual beds show clear normal and, in one case, inverse graded bedding, generally varying from coarse sand to coarse silt. The thickness of graded beds varies from <10 cm to 0.95 m.

Volcaniclastic and pumiceous sand beds generally have sharp contacts with underlying layers but gradational contacts with overlying units, indicating a waning sediment supply. This observation is consistent with deposition from a gravity flow, probably resulting from episodic volcanic and seismic activity within and around the area, coupled with the instability of volcanic flanks in this region. The bulk mineralogy of these sediments is volcanic glass, anorthite, quartz, albite, muscovite, and trace amounts of microline and augite, based on microscopic and XRD examinations (Table T3). Shards of volcanic glass are usually brown and yellow-brown and are poorly sorted, ranging in size from coarse sand to pebbles as large as 1.2 cm in diameter. Vesicular structure is well

developed on the surface of the volcanic glass shards, and pores are somewhat elongate and filled with diagenetic white minerals.

Biostratigraphy

Core catcher samples from Site C0017 yielded two zones with microfossils, a shallow one from ~9 to 28 mbsf and a deeper one from ~112 to 145 mbsf (Table T4). The upper layer consists of pumice and microfossils, which are most abundant in the deeper half of this interval (at ~18.5 and 27.2 mbsf). These two samples each possess a large fraction of <63 µm material. Foraminiferal diversity and abundance are generally consistent with surface samples from a similar pumice-foraminifer layer at Site C0014, suggesting it is a modern assemblage. Examination of wet mounts of the <63 µm material using phase contrast microscopy ± cross-polarized light revealed good preservation of coccoliths. The assemblage was dominated by *Emiliania huxleyi*, *Gephyrocapsa oceanica*, and *Reticulofenestra asanoi*, highlighting a modern origin (Raffi et al., 2006; Winter and Siesser, 1994). Transport of coccoliths into the upper microfossil zone was facilitated, in part, by fecal pellets (Fig. F5). Fecal pellets and abundant centric diatoms are notable in the sample from 10.6 mbsf.

Drilling continued through a pumice-rich layer from which core recovery was poor (Table T4) before entering a second interval characterized by microfossils (~112–138 mbsf). This deeper zone of microfossils is also characterized by a large fraction of <63 µm material. Coccoliths at these depths (*E. huxleyi* and *R. asanoi*) are poorly preserved and much less abundant (<10%) than they are in the upper layer (8–28 mbsf). Foraminiferal abundances in this layer are also lower than in the upper, modern zone; however, there is a larger proportion (as high as 11%) of benthic foramininfers in the 125 mbsf region. The large proportion of benthic foraminifers suggests the site was more favorable to benthic species in the past than it is today (i.e., hydrothermal activity may have increased at the site).

As at Site C0014, foraminifers observed in both of these layers (~8–28 and 112–138 mbsf) are dominated by planktonic species (Table T5), suggesting a large input of planktonic foraminifers and/or that Site C0017 is a poor habitat for benthic foraminifers (Saidova, 2007), perhaps because it is still too close to the hydrothermal system. Though some fragmentation has occurred, foraminiferal preservation is generally good, with little or no evidence for dissolution and/or overgrowth; diagnostic characteristics are preserved, and many species can be identified. As at Site C0014, the abundance of *Neogloboquadrina pachyderma* dextral relative to the sinistrally coiled subspecies demonstrates the influence of warmer waters, presumably from the Kuroshio Current (Bandy, 1960; Ericson, 1959). Some foraminifers from 112 mbsf are pyritized (not shown), consistent with previous reports describing infilling of foraminiferal tests (Kohn et al., 1998). It should be noted that these foraminifers are poorly preserved compared with those at Site C0014 (see Figs. F11 and F12 in Expedition 331 Scientists, 2011d).

Petrology

Site C0017, which was one of the contingency sites for Expedition 331, targeted a potential recharge zone ~1.5 km east of the principal hydrothermal field at Iheya North Knoll. Four holes were drilled within a 10 m radius (Fig. F1) at Site C0017, where the intervals from 0.0 to 37.3 mbsf (Holes C0017A–C0017C) and 60 to 150.7 mbsf (Hole C0017D) were cored. The four holes are considered to represent a single drilled section for purposes of petrological interpretation.

Hydrothermal alteration

The sequence drilled at Site C0017 comprises calcareous clay, volcaniclastic and foraminiferal silt and sand, and pumiceous grit and gravel (see **"Lithostratigraphy"**). With the exception of two intervals discussed below and the weak scattered development of green staining of pumice fragments in the upper parts of the sequence (interpreted as glauconitic "greensand," although glauconite was not identified by XRD), the extensive hydrothermal alteration seen at Sites C0013 and C0014 is almost absent in the drilled interval at Site C0017.

In Hole C0017C, the interval from ~26 to 35 mbsf (Sections 331-C0017-1H-6 through 2H-6) shows weak to moderate oxidation, similar in nature but more intense than that seen at Site C0015. Oxidation is expressed as yellow to brown coloration of clay, silt, and sand, the development of orange to brown iron oxide staining on pumice fragments (Fig. F6), and the occurrence of 1–2 mm orange-brown botryoidal aggregates of Fe-Si oxyhydroxides. XRD analyses of samples from this interval show similar mineral assemblages to those that were identified for unaltered material from the site (see below), with the exception that primary igneous feldspar is absent in some samples. It is likely that some degree of feldspar destruction accompanies the oxidation of the pumice. Geochemical results (see **"Geochemistry"**) indicate that this zone of oxidation within the otherwise reduced sedimentary sequence is the result of an influx of seawater at this depth, potentially repre-

senting recharge flow into the Iheya North hydrothermal system.

The only other visual evidence of hydrothermal alteration at Site C0017 was seen in Core 331-C0017D-11X (140.2–149.7 mbsf), the deepest core from the site, which shows development of pale gray clay alteration of more permeable pumiceous grit horizons, intercalated with apparently unaltered indurated dark gray calcareous clay (Fig. F7). XRD analyses of this altered material (Table T3) identify the same quartz-glass ± anorthite assemblage as for unaltered pumiceous horizons (consistent with the visual observation that much of the pumice retains its original texture and mineralogy), with the addition of sylvite and halite in one sample (see "Mineralogy and pore fluid chemistry," below).

The remaining sequence drilled at Site C0017 shows no visual evidence of alteration, with routine XRD identifying those phases that would be expected for a sequence of calcareous and volcaniclastic marine sediments, namely calcite, dolomite (discussed in "Mineralogy and pore fluid chemistry," below), quartz, feldspar, muscovite, chlorite, and volcanic glass (Table T3). Halite is also commonly detected using XRD in samples from below ~25 mbsf, but it is possible that this may be due to seawater contamination from drilling.

Sulfide mineralization

When compared with Sites C0013 and C0014, the drilled interval at Site C0017 is notable for the absence of sulfide mineralization at shallow depth. Pyrite was only observed consistently at depths below 94 mbsf in Hole C0017D. In these deeper portions of the sequence, pyrite occurs in trace quantities as very fine grained disseminations and as rare scattered 1–3 mm aggregates with quartz and occasional discontinuous millimeter-scale bands or veins within indurated clay sediment.

Mineralogy and pore fluid chemistry

Site C0017 is the only location cored during Expedition 331 where dolomite is present in sediments (it also occurs in anhydrite nodules at Site C0013). At Site C0017, the occurrence of dolomite is limited to two discrete depth intervals (Table T3): ~10–20 mbsf in Holes C0017B and C0017C and ~110–140 mbsf in Hole C0017D. These intervals correlate well with intervals of low-Mg, high-alkalinity pore fluids (Figs. F8, F9; see "Geochemistry").

The detection of the evaporitic minerals sylvite (KCl) and halite at ~143 mbsf in Sample 331-C0017D-11X-3, 27–29 cm, also correlates well with the pore water chemistry, corresponding to a sharp increase in dissolved K at that depth (Fig. F8; see "Geochemistry").

Geochemistry

Interstitial water

A total of 21 whole-round samples were processed at Site C0017 from four different holes (Table T6). Many samples were collected immediately above or below whole rounds dedicated for microbiology; however, there were more whole rounds collected for interstitial water analyses than for microbiology at this site. We squeezed whole rounds at the laboratory temperature of ~20°C rather than at in situ temperature. More than half of the samples are from Hole C0017D, from 63 to 141 mbsf.

Major and minor cations and anions

Na concentrations (Fig. F8) are nearly constant with depth, whereas Cl (Fig. F10) increases, yielding a small decrease in Na/Cl in Hole C0017D relative to the shallower holes. Potassium is generally above seawater concentrations in the uppermost 10–20 mbsf, probably because of irreversible ion exchange with clays, but it decreases to below seawater values below ~70 mbsf and then increases again to seawater concentration in the bottommost 10 m of Hole C0017D. The decrease likely results from uptake into alteration minerals at low temperature, but the increase requires a source of potassium near the bottom of the hole. One possible source is dissolution of sylvite (KCl), which was reported in the core at 143 mbsf (see "Mineralogy and pore fluid chemistry"). A second possible source is lateral incursion of a K-rich solution at this depth, which could be either seawater or a high-temperature hydrothermal solution. Seawater incursion would increase K but would also increase Mg and lower Ca, and neither of these changes is observed; a hydrothermal solution therefore seems more likely. Enrichments in Ca at depth are consistent with sediment alteration and release of Ca to the pore water. Mg is slightly depleted in both the upper and lower 20 m of the hole. These slight depletions coincide with the presence of dolomite in the corresponding intervals, at 10–20 and 110–140 mbsf (Table T3). Distributions of B, Li, and Sr are likewise consistent with low-temperature weathering deep in the sequence (Fig. F11). Like K, Li is higher than in seawater within the uppermost 20 mbsf.

Sulfate, alkalinity, ammonium, phosphate, and silicon

Sulfate displays a minimum concentration at 15 mbsf (Fig. F10) that roughly coincides with maxima in alkalinity, ammonium, phosphate, and Si at 11–

15 mbsf (Fig. F9) and likely results from sulfate reduction coupled with oxidation of organic matter in the sediments. Sulfate increases again to slightly in excess of seawater concentration below 15 mbsf and is roughly uniform at greater depth, with some scatter. As interpreted in "Petrology," the increase in sulfate at ~25 mbsf, along with the accompanying decreases in alkalinity, ammonium, phosphate, manganese, and silicon, almost certainly results from lateral intrusion of unaltered ocean bottom water into the sediment at ~30 mbsf. Below this zone of seawater intrusion, phosphate remains low. Alkalinity exhibits some structure below 50 mbsf, increasing significantly below ~75 mbsf, probably because of low-temperature alteration reactions. Silica generally decreases with depth, suggesting some uptake into authigenic minerals and/or a second deep zone of seawater recharge. This constituent scatters about concentrations that are lower than those found at Sites C0013 and C0014 (Fig. F9).

Summary

The uppermost 25–35 m at Site C0017 is characterized by organic matter diagenesis in the upper half and intrusion of seawater in the lower half. Below ~50 mbsf, this site is characterized by low-temperature alteration reactions and considerable scatter in the pore water data, probably resulting from interaction between chemical and hydrologic processes. The shape of the temperature profile indicates overall downwelling at Site C0017, with irregularities suggestive of nonsteady-state processes including lateral flow. The temperature gradient increases from 70 to 80 mbsf, becomes nearly flat at 85–110 mbsf, and increases again to 90°C at the bottom of the hole (see "Physical properties"), suggesting a complex three-dimensional hydrologic regime on which are superimposed the effects of temperature-dependent water-rock reactions.

Headspace gas analysis

Methane concentrations (Fig. F12) are quite low, mostly <1 µM. The highest values are near the bottom of the deepest Hole C0017D, where a mean value of 1.8 µM was found between 112 and 141 mbsf. The highest concentration is 3.4 µM at 112 mbsf. Methane measured in safety gas (Table T7) and science gas samples (Table T8) shows similar trends, but science gas analyses had a higher detection limit because the gas chromatograph used shows a large nitrogen peak near the methane peak. Science gas samples are thus mostly below detection, except for samples at ~137 mbsf, which show 1–2 µM methane. We conclude that methanogensis is not a robust metabolism at Site C0017. The small concentration of methane in pore water from deep horizons (112–137 mbsf) may be hydrothermal in origin or it may result from methanogenesis occurring deep at this site.

Hydrogen was not observed except for small peaks at six horizons scattered down the sediment column (Table T8).

Sediment carbon, nitrogen, and sulfur composition

Calcium carbonate ($CaCO_3$) content calculated from inorganic carbon concentration ranges from 44.77 wt% to below the detection limit (<0.001 wt%) (Table T9; Fig. F13). High concentrations (>5 wt%) were observed at depths above 25 mbsf, where the sediment is mostly hemipelagic clay containing foraminiferal shells (see "Lithostratigraphy"). The highest $CaCO_3$ contents (>40 wt%) were observed in calcareous sand and sandy clay layers, which contain a large amount of foraminiferal shells. $CaCO_3$ contents are low at 25–80 mbsf, where the sediment is mostly pumiceous gravel. $CaCO_3$ averages 6 wt% below 95 mbsf, where the sediment is hemipelagic clay with sandy layers, the same lithology as that within the uppermost 25 m.

Total organic carbon (TOC) content ranges from 0.01 to 0.96 wt% (Fig. F14). High concentrations (>0.5 wt%) were observed at depths above 25 mbsf, although layers of volcaniclastic sand within this depth interval have low concentrations (0.1 to ~0.3 wt%). TOC content is generally low (<0.1 wt%) in pumiceous sediments between 25 and 80 mbsf. Below 95 mbsf, it averages 0.3 wt%. Total nitrogen (TN) ranges from below the detection limit (<0.001 wt%) to 0.11 wt%. TN is higher in the hemipelagic sediment at 0–25 and below 95 mbsf than it is in pumiceous sediments between 25 and 95 mbsf. The ratio of TOC to TN (C/N) in hemipelagic sediments is generally larger than the Redfield ratio of 6.6, indicating an organic origin for nitrogen. Values smaller than the Redfield ratio, especially in pumiceous sediments, indicate that some portion of TN is inorganic.

Total sulfur (TS) content ranges from 0.03 to 0.7 wt%. TS is generally low (<0.2 wt%) in the pumiceous sediment between 25 and 80 mbsf. Total sulfur is lower at Site C0017 than at Sites C0013, C0014, and C0016, where significant amounts of hydrothermal sulfide and sulfate were observed.

Microbiology

Total prokaryotic cell counts

The abundance of microbial cells in subseafloor sediments at Site C0017 was evaluated by fluorescent microscopy using SYBR Green I as a fluorochrome dye.

Maximum cell numbers were observed at 6.36 mbsf (3.2×10^7 cells/mL), and cell numbers range from 2.4 × 10^7 to 3.2 × 10^7 cells/mL at depths above 10.8 mbsf. Microbial cell counts irregularly decrease with depth (Fig. **F15;** Table **T10**). Below 50 mbsf, cell counts decrease to less than the limit of detection of ~1 × 10^6 to 4 × 10^6 cells/mL.

Cultivation of thermophiles

Growth of *Thermococcales* (e.g., *Thermococcus*) at 80°C and *Aquificales* (e.g., *Persephonella*) and thermophilic *Epsilonproteobacteria* (e.g., *Nitratiruptor*) at 55°C was examined for cores from a high-temperature zone below 94.7 mbsf. No growth of thermophiles was observed on board.

Contamination tests

Fluorescent microspheres and perfluorocarbon tracer (PFT) were used to test for contamination (Tables **T11, T12**). The PFT test suggests that even in sediment layers containing large amounts of pumice, contamination by drilling fluid was quite low. This was the case even at the outer surface of the core and even with larger grain sizes, which have the greatest risk of contamination. We found evidence for contamination by drilling fluid in the interior of cores obtained from Hole C0017D by the ESCS, but detected PFT concentrations were much lower than those in the drilling mud fluid collected from the onboard tank and that adhering to the massive sulfide of Site C0016 (Table **T12;** see Table **T8** in Expedition 331 Scientists, 2011b, and Table **T6** in Expedition 331 Scientists, 2011f).

Cultivation of iron-oxidizing bacteria

The depth interval from ~26 to 35 mbsf at Site C0017 probably represents a zone of recharge flow in this hydrothermal system, as suggested by the temperature and pore water chemistry profiles (see **"Petrology"** and **"Geochemistry"**). It looks to be heavily oxidized, by either biotic or abiotic means. The interaction of infiltrating cold seawater with the surrounding reduced layers would produce a redox boundary that can be utilized by many microorganisms, including iron-oxidizing bacteria. For this reason we targeted this oxidized interval for FeOB cultivation experiments (Table **T13**). Samples 331-C0017C-1H-7, 1 cm, and 1H-7, 2 cm, are two subsamples from the same whole round, but the latter is more rust-colored and appears to be more oxidized.

After 4.5 days of growth, samples from the top of this depth interval, in a section of iron oxide–stained pumice fragments at 26.26–28.45 mbsf, showed significant growth in artificial seawater (ASW) media A (microaerophilic). The preference of these microbes for a microaerophilic environment agrees with the identification of this layer as a zone of recharge flow (oxygenated seawater). Above this layer, outside of the oxidized zone, little to no growth of FeOB was observed. Below this layer, where the sediments transition from yellow-to-brown clay, silt, and sand (see **"Petrology"**), there was also no growth, suggesting a FeOB preference for growth where there is less fine-grained material.

Observations of putative FeOB cellular morphology were similar to those from other sites from Expedition 331. These include ~1.5 µm rod-shaped cells associated with small particles (Fig. **F16A, F16B, F16E, F16F**) in addition to large aggregates of cells colonizing larger particles (possibly iron oxides; Fig. **F16G, F16H**). Of particular importance are the two cells localized on the end of a stalklike structure (Fig. **F16C, F16D**). Though difficult to see because of the angle of observation, moving up and down through the plane of focus showed that these cells were on opposite sides of a stalk jutting out of the top of the larger particle. This is the first observation of a putative bifurcated iron oxide twisted stalk with attached cells in any of the incubations viewed during the expedition.

Contamination tests from Site C0017 (Tables **T11, T12**) reveal that all samples that showed growth also exhibited some level of contamination. For Section 331-C0017C-1H-7, contamination was below detection after counting 100 fields, though a single bead was seen upon cursory examination. This may be due to a cracked core liner for that section allowing washout to have occurred. Section 331-C0017C-1H-6 was taken after this core was split and was not tested for contamination, though it came from an intact internal location within the core. Overall, caution must still be exercised when considering whether these Site C0017 enrichments represent FeOB originating from in situ locations.

In an attempt to test whether biotic iron oxidation was occurring in situ at depth, the original sample used to inoculate the enrichment for Section 331-C0017C-1H-7 was dried and imaged using the scanning electron microscope (SEM) and analyzed with energy dispersive spectrometry (EDS) to test for the presence of putative iron oxide filaments of biotic origin. As the doubling time for FeOB is ~12 h (Emerson et al., 2007), these filaments would not have had time to form as the core was brought on deck. SEM results show a number of patches of iron and iron oxide filaments, many located within protected cavities of pumice fragments. Photos were taken of filaments within these cavities (Fig. **F17A, F17B**), which may explain the lack of a significant oxygen peak in

the EDS spectrum. Figure F17C is the only EDS spectrum that has a significant oxygen peak; however, because of the low ratio of oxygen to iron, an iron oxyhydroxide (FeOOH) filament is improbable as compared to other marine FeOB (Emerson and Moyer, 2002; Emerson et al., 2007). Though it is possible that all three of these iron/iron oxide filament patches are of biotic origin, this evidence is not conclusive. Further testing must be conducted onshore.

Conclusions

Site C0017 is located in a probable seawater recharge area in the Iheya North field. Significant impacts of hydrothermal fluids were not observed in geochemical profiles and sediment alteration, except for localized oxidation (see "Geochemistry" and "Lithostratigraphy"). The temperature at the bottom of the deepest Hole C0017D at 151 mbsf is 90°C. We have thus had an opportunity to observe subseafloor microbial communities likely supported by buried organic matter, over a considerable range of temperature.

Relatively low microbial abundance compared with previous Ocean Drilling Program/IODP sites on continental margins (Parkes et al., 1994, 2000; D'Hondt et al., 2004) was seen at Site C0017 (as many as 3.2×10^7 cells/mL), as was also the case at Site C0015 (as many as 1.2×10^7 cells/mL). Cell abundance at Site C0017 may also be depressed as a result of the generally low levels of organic carbon available in the subseafloor sediments around the Iheya North field (see "Microbiology" and "Geochemistry," both in Expedition 331 Scientists, 2011e). At Site C0017, effects of lithology on cell abundance were again observed, as at Site C0015, where a relatively abundant microbial biomass was observed in samples with pumiceous sands and gravels. (Compare, for example, cell counts in the pumiceous sample from 10.8 mbsf in Hole C0017B with that in the hemipelagic mud sample from 14.8 mbsf) (Table T10). As is usually the case (Parkes et al., 1994, 2000), the subseafloor microbial abundance generally decreases with depth (Fig. F15). Lithostratigraphy at Site C0017 consists of diverse units such as hemipelagic mud and clay, pumiceous sediment, and volcaniclastic-pumiceous mixed sand (see "Lithostratigraphy"). Cell abundances are strongly influenced by this lithological variation and its effect on porosity and pore space size, as seen in previous studies (Schmidt et al., 1998; Zhang et al., 1998; Parkes et al., 2000; Inagaki et al., 2003; Rebata-Landa and Santamarina, 2006), as well as by geochemical constraints imposed by seawater recharge.

Though contamination cannot be ruled out, enrichment experiments represent the deepest successful FeOB enrichments to date in a marine environment and could lend insight into the colonization of low-temperature hydrothermal systems via recharge zone flow.

Physical properties

Physical property measurements were made at Site C0017 to nondestructively characterize lithological units and states of sediment consolidation. In the following discussion, the four holes at Site C0017 (Holes C0017A, C0017B, C0017C, and C0017D) are treated as one continuous depth profile.

Density and porosity

Bulk density at Site C0017 was determined from both gamma ray attenuation (GRA) measurements on whole cores (with the multisensor core logger for whole-round samples [MSCL-W]) and moisture and density (MAD) measurements on discrete samples (see "Physical properties" in Expedition 331 Scientists, 2011b). A total of 70 discrete samples were analyzed for MAD (7, 9, 14, and 40 from Holes C0017A, C0017B, C0017C, and C0017D, respectively). Wet bulk density is roughly constant with depth to ~20 mbsf (Holes C0017A and C0017B) (Fig. F18; Table T14), as determined by both MAD and GRA, although the latter values are generally lower than the former and exhibit more scatter than previous sites. The average bulk density in Holes C0017A and C0017B is ~1.59 g/cm^3. Between 20 and 60 mbsf (Hole C0017C), bulk density decreases somewhat from ~1.7 to 1.3 g/cm^3. In Hole C0017D, bulk density is relatively constant from 60 to 80 mbsf (~1.5 g/cm^3) and then increases to ~1.9 g/cm^3 between 80 and 147 mbsf.

Grain density was calculated from discrete MAD measurements and is also approximately constant (2.6 ± 0.2 g/cm^3) between 0 and 80 mbsf (data not shown). Grain density is slightly lower than average in the depth range from ~30 to 80 mbsf.

Porosity was calculated from MAD measurements. It is generally quite high (~60%) and mirrors patterns of bulk density. It is relatively constant in Holes C0017A and C0017B; it increases somewhat between 20 and ~80 mbsf (Hole C0017C and the upper part of Hole C0017D) and then decreases steadily toward values between 20% and 30% at the bottom of Hole C0017D (~147 mbsf) (Fig. F19; Table T14).

Density and porosity results from the four holes at Site C0017 reflect the basic lithology of the hole. In the uppermost 20 m, sediments are predominantly clays with some sand and pumice; between 20 and 80 mbsf is a higher incidence of pumice and corre-

spondingly lower bulk density. From 95 to 145 mbsf, sediments are again dominated by clays and the density increases. At finer scales in the clay-dominated sections, GRA-derived density and MSCL-derived *P*-wave velocities exhibit small changes that reflect changes from finer grained clays to somewhat coarser grained silty clays (see **"*P*-wave velocity and anisotropy measurements"**).

Electrical resistivity (formation factor)

Formation factor is a measure of the connected pore space within sediment and is used to calculate the bulk sediment diffusion coefficient. Electrical impedance measurements were made at 87 depths (13, 14, 13, and 47 measurements in Holes C0017B, C0017C, C0017D, and C0017E, respectively). Formation factors calculated for Hole C0017 are near 3 in the uppermost 30 mbsf (Holes C0017A and C0017B); values increase with depth and are generally between ~5 and 8 (Fig. **F20**). Several peaks in formation factor generally occur where sediment water content is lower (bulk density is higher), but the peaks are not clearly related to any lithostratigraphic control and may be measurement artifacts.

P-wave velocity and anisotropy measurements

P-wave velocity and relative anisotropy were measured on discrete samples indurated enough to cut sample polyhedrons. This was rarely the case. MSCL-derived *P*-wave velocities generally increase with depth in the core as sediments become more compacted (Fig. **F21**). It is not always clear from the lithology what causes some of the larger peaks in *P*-wave velocity; however, small-scale variations often correlate with changes in grain size and density.

Thermal conductivity

Thermal conductivity was measured on whole-round cores. A total of 88 measurements were made (13, 15, 14, and 46 measurements from Holes C0017A, C0017B, C0017C, and C0017D, respectively). Average thermal conductivity in Holes C0017A and C0017B is ~1 W/(m·K). Between 20 and 60 mbsf (Hole C0017C), thermal conductivity decreases somewhat sharply from ~1 to 0.3 W/(m·K). In Hole C0017D it increases from ~0.5 W/(m·K) at 65 mbsf to 1.5 W/(m·K) between 120 and 140 mbsf (Fig. **F22**). Average thermal conductivity for all four holes is 1.09 ± 0.3 W/(m·K). Thermal conductivity is loosely and inversely correlated with porosity. As porosity decreases, thermal conductivity increases as water is forced from void spaces, because the thermal conductivity of grains is greater than that of water.

In situ temperature

In situ temperature was measured using the APCT3 (six of eight measurements were successful, at 18–112 mbsf) and thermoseal strips (one measurement at 151 mbsf) (Table **T15;** Fig. **F23**). For the APTC3, all temperature-time series were recorded at 1 s intervals. The APCT3 stopped at the mudline for as long as 10 min prior to each penetration, yielding eight measurements of bottom water temperature that averaged 4.87° ± 0.51°C (1σ). This range indicates that strong bottom water temperature variation exists, spatially, temporally, or both. Temperature-time series for each measurement are shown in Figure **F24.** Temperature records show significant frictional heating as the coring shoe penetrated the sediment, followed by subsequent temperature decay toward the in situ value. For most of the measurements, the probe was kept in the sediment for >5 min, allowing accurate extrapolation to equilibrium formation temperature based on a 1/time approximation (Table **T15**). Most measurements exhibit good penetration heating and initial decay curves, with two exceptions: Core 331-C0017D-4H at 84.7 mbsf, which did not have good penetration, and Core 12H at 150.7 mbsf, where recorded temperatures are greater than the calibrated maximum temperature for the APCT3 tool (55°C). Mathematical fits to the temperature-time series are also good and yield the equilibrium formation temperatures that are plotted versus depth in Figure **F23.** The deepest measurement at 150.7 mbsf was determined from three replicate thermoseal strips, with beads calibrated to blacken when exposed to temperatures of 75°, 80°, 85°, 90°, and 95°C. The first four beads were blackened on two of the strips, indicating exposure to a temperature between 90° and 95°C, and the first three beads were blackened on the third strip indicating a temperature between 85° and 90°C. We report this temperature somewhat conservatively as 90° ± 5°C.

Temperature and thermal conductivity at Site C0017 vary from one lithological unit to another (Fig. **F24**). Three broad units can be defined: from the top to 60 mbsf (Unit I), from 60 to 100 mbsf (Unit II), and from 100 mbsf to the bottom (Unit III). These correspond roughly with the upper clay layers, the middle pumice-rich layers, and the hard, indurated clay layers defined by the MAD data and the lithostratigraphy results.

Heat flow

If heat transfer proceeds via conduction and heat flow is constant, the thermal gradient is inversely proportional to thermal conductivity according to Fourier's law (Expedition 331 Scientists, **2011b**). Heat flow was estimated using the mean thermal

conductivity derived for each unit (I, II, and III) (Table T16). Values increase by roughly a factor of 10 within each unit.

MSCL-I and MSCL-C imaging

MSCL-derived core images and color analyses are presented in the visual core descriptions (VCDs).

MSCL-W derived electrical resistivity

MSCL-W based resistivity data at this site are generally low (<4 Ωm), but there are regions of high resistivity at ~37 mbsf (5–30 Ωm) and at 95 and 140 mbsf (10–20 Ωm). There is no obvious relationship with the discrete measurements of formation factor (Fig. F25 versus Fig. F20).

References

Bandy, O.L., 1960. The geologic significance of coiling ratios in the foraminifer *Globigerina pachyderma* (Ehrenberg). *J. Paleontol.,* 34(4):671–681. **http://jpaleontol.geoscienceworld.org/cgi/content/abstract/34/4/671**

D'Hondt, S., Jørgensen, B.B., Miller, D.J., Batzke, A., Blake, R., Cragg, B.A., Cypionka, H., Dickens, G.R., Ferdelman, T., Hinrichs, K.-U., Holm, N.G., Mitterer, R., Spivack, A., Wang, G., Bekins, B., Engelen, B., Ford, K., Gettemy, G., Rutherford, S.D., Sass, H., Skilbeck, C.G., Aiello, I.W., Guerin, G., House, C.H., Inagaki, F., Meister, P., Naehr, T., Niitsuma, S., Parkes, R.J., Schippers, A., Smith, D.C., Teske, A., Wiegel, J., Naranjo Padillo, C., and Solis Acosta, J.L., 2004. Distributions of microbial activities in deep subseafloor sediments. *Science,* 306(5705):2216–2221. **doi:10.1126/science.1101155**

Emerson, D., and Moyer, C.L., 2002. Neutrophilic Fe-oxidizing bacteria are abundant at the Loihi Seamount hydrothermal vents and play a major role in Fe oxide deposition. *Appl. Environ. Microbiol.,* 68(6):3085–3093. **doi:10.1128/AEM.68.6.3085-3093.2002**

Emerson, D., Rentz, J.A., Lilburn, T.G., Davis, R.E., Aldrich, H., Chan, C., and Moyer, C.L., 2007. A novel lineage of *Proteobacteria* involved in formation of marine Fe-oxidizing microbial mat communities. *PLoS ONE,* 2(8):e667. **doi:10.1371/journal.pone.0000667**

Ericson, D.B., 1959. Coiling direction of *Globigerina pachyderma* as a climatic index. *Science,* 130(3369):219–220. **doi:10.1126/science.130.3369.219**

Expedition 331 Scientists, 2011a. Expedition 331 summary. *In* Takai, K., Mottl, M.J., Nielsen, S.H., and the Expedition 331 Scientists, *Proc. IODP,* 331: Tokyo (Integrated Ocean Drilling Program Management International, Inc.). **doi:10.2204/iodp.proc.331.101.2011**

Expedition 331 Scientists, 2011b. Methods. *In* Takai, K., Mottl, M.J., Nielsen, S.H., and the Expedition 331 Scientists, *Proc. IODP,* 331: Tokyo (Integrated Ocean Drilling Program Management International, Inc.). **doi:10.2204/iodp.proc.331.102.2011**

Expedition 331 Scientists, 2011c. Site C0013. *In* Takai, K., Mottl, M.J., Nielsen, S.H., and the Expedition 331 Scientists, *Proc. IODP,* 331: Tokyo (Integrated Ocean Drilling Program Management International, Inc.). **doi:10.2204/iodp.proc.331.103.2011**

Expedition 331 Scientists, 2011d. Site C0014. *In* Takai, K., Mottl, M.J., Nielsen, S.H., and the Expedition 331 Scientists, *Proc. IODP,* 331: Tokyo (Integrated Ocean Drilling Program Management International, Inc.). **doi:10.2204/iodp.proc.331.104.2011**

Expedition 331 Scientists, 2011e. Site C0015. *In* Takai, K., Mottl, M.J., Nielsen, S.H., and the Expedition 331 Scientists, *Proc. IODP,* 331: Tokyo (Integrated Ocean Drilling Program Management International, Inc.). **doi:10.2204/iodp.proc.331.105.2011**

Expedition 331 Scientists, 2011f. Site C0016. *In* Takai, K., Mottl, M.J., Nielsen, S.H., and the Expedition 331 Scientists, *Proc. IODP,* 331: Tokyo (Integrated Ocean Drilling Program Management International, Inc.). **doi:10.2204/iodp.proc.331.106.2011**

Inagaki, F., Suzuki, M., Takai, K., Oida, H., Sakamoto, T., Aoki, K., Nealson, K.H., and Horikoshi, K., 2003. Microbial communities associated with geological horizons in coastal subseafloor sediments from the Sea of Okhotsk. *Appl. Environ. Microbiol.,* 69(12):7224–7235. **doi:10.1128/AEM.69.12.7224-7235.2003**

Kohn, M.J., Riciputi, L.R., Stakes, D., and Orange, D.L., 1998. Sulfur isotope variability in biogenic pyrite: reflections of heterogeneous bacterial colonization? *Am. Mineral.,* 83(11–12):1454–1468. **http://www.minsocam.org/msa/ammin/TOC/Articles_Free/1998/Kohn_p1454-1468_98.pdf**

Parkes, R.J., Cragg, B.A., Bale, S.J., Getliff, J.M., Goodman, K., Rochelle, P.A., Fry, J.C., Weightman, A.J., and Harvey, S.M., 1994. Deep bacterial biosphere in Pacific Ocean sediments. *Nature (London, U. K.),* 371(6496):410–413. **doi:10.1038/371410a0**

Parkes, R.J., Cragg, B.A., and Wellsbury, P., 2000. Recent studies on bacterial populations and processes in subseafloor sediments: a review. *Hydrogeol. J.,* 8(1):11–28. **doi:10.1007/PL00010971**

Raffi, I., Backman, J., Fornaciari, E., Pälike, H., Rio, D., Lourens, L., and Hilgen, F., 2006. A review of calcareous nannofossil astrobiochronology encompassing the past 25 million years. *Quat. Sci. Rev.,* 25(23–24):3113–3137. **doi:10.1016/j.quascirev.2006.07.007**

Rebata-Landa, V., and Santamarina, J.C., 2006. Mechanical limits to microbial activity in deep sediments. *Geochem., Geophys., Geosyst.,* 7(11):Q11006–Q11017. **doi:10.1029/2006GC001355**

Saidova, K.M., 2007. Benthic foraminiferal assemblages of the South China Sea. *Oceanology,* 47(5):653–659. **doi:10.1134/S0001437007050074**

Schmidt, J.L., Deming, J.W., Jumars, P.A., and Keil, R.G., 1998. Constancy of bacterial abundance in surficial marine sediments. *Limnol. Oceanogr.,* 43(5):976–982. **doi:10.4319/lo.1998.43.5.0976**

Weigland, P.W., Matthews, V., III, Cornelius, S., and Talbot, J., 2003. Origin of green color in lapilli tuff from the Pinnacles Volcanic Formation, California. *Geol. Soc. Am.*

Abstr. Progr., 35(6):579. **http://gsa.confex.com/gsa/2003AM/finalprogram/abstract_64025.htm**

Winter, A., and Siesser, W.G., 1994. Atlas of living coccolithophores. *In* Winter, A., and Siesser, W.G. (Eds.), *Coccolithophores:* Cambridge (Cambridge Univ. Press), 107–159.

Zhang, C., Palumbo, A.V., Phelps, T.J., Beauchamp, J.J., Brockman, F.J., Murray, C.J., Parsons, B.S., and Swift, D.J.P., 1998. Grain size and depth constraints on microbial variability in coastal plain subsurface sediments. *Geomicrobiol. J.,* 15(3):171–185. **doi:10.1080/01490459809378074**

Publication: 4 October 2011
MS 331-107

Figure F1. Bathymetric map, Site C0017.

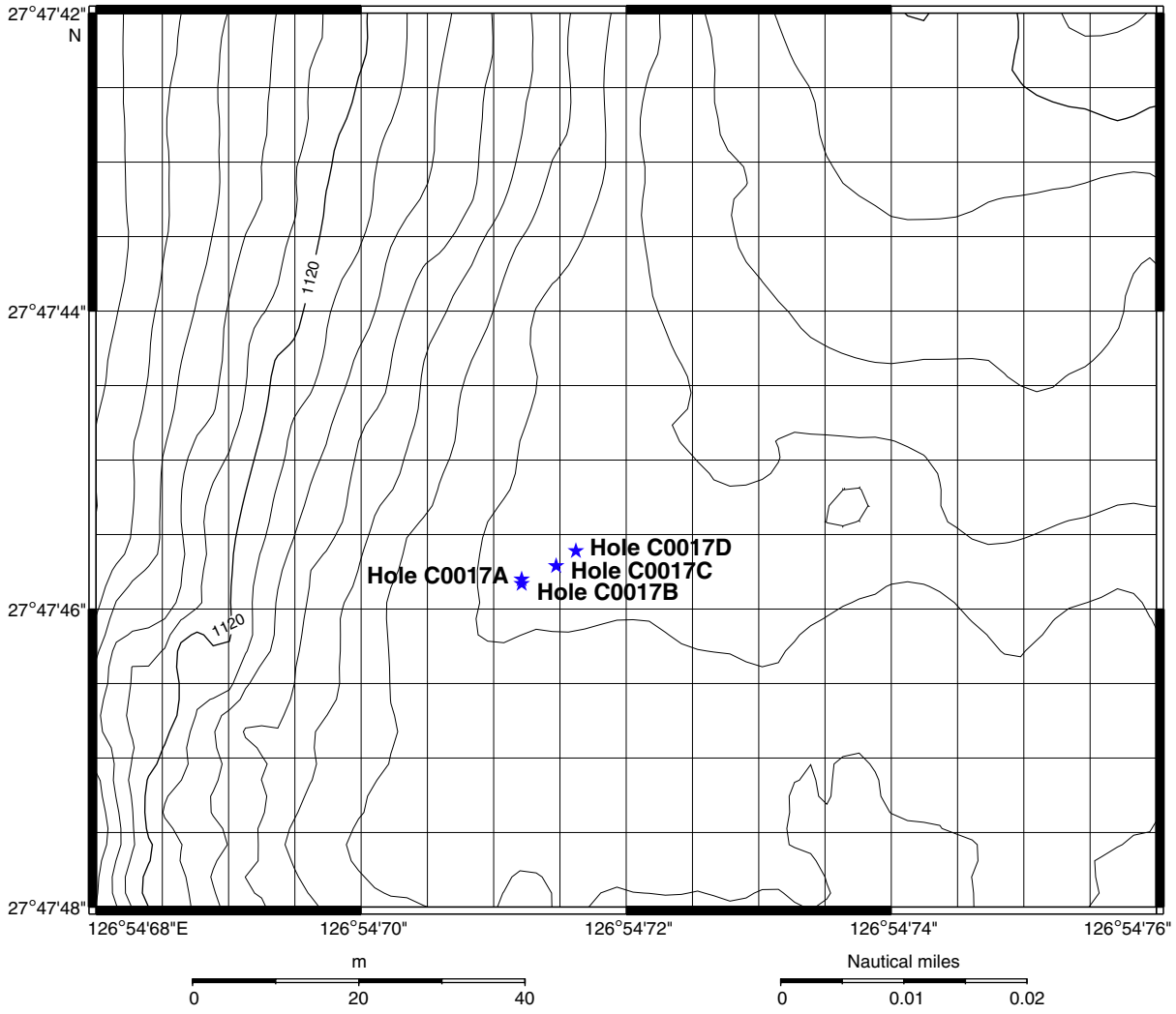

Figure F2. Sedimentary log for Site C0017, showing sediment types and lithological units, as defined in the text.

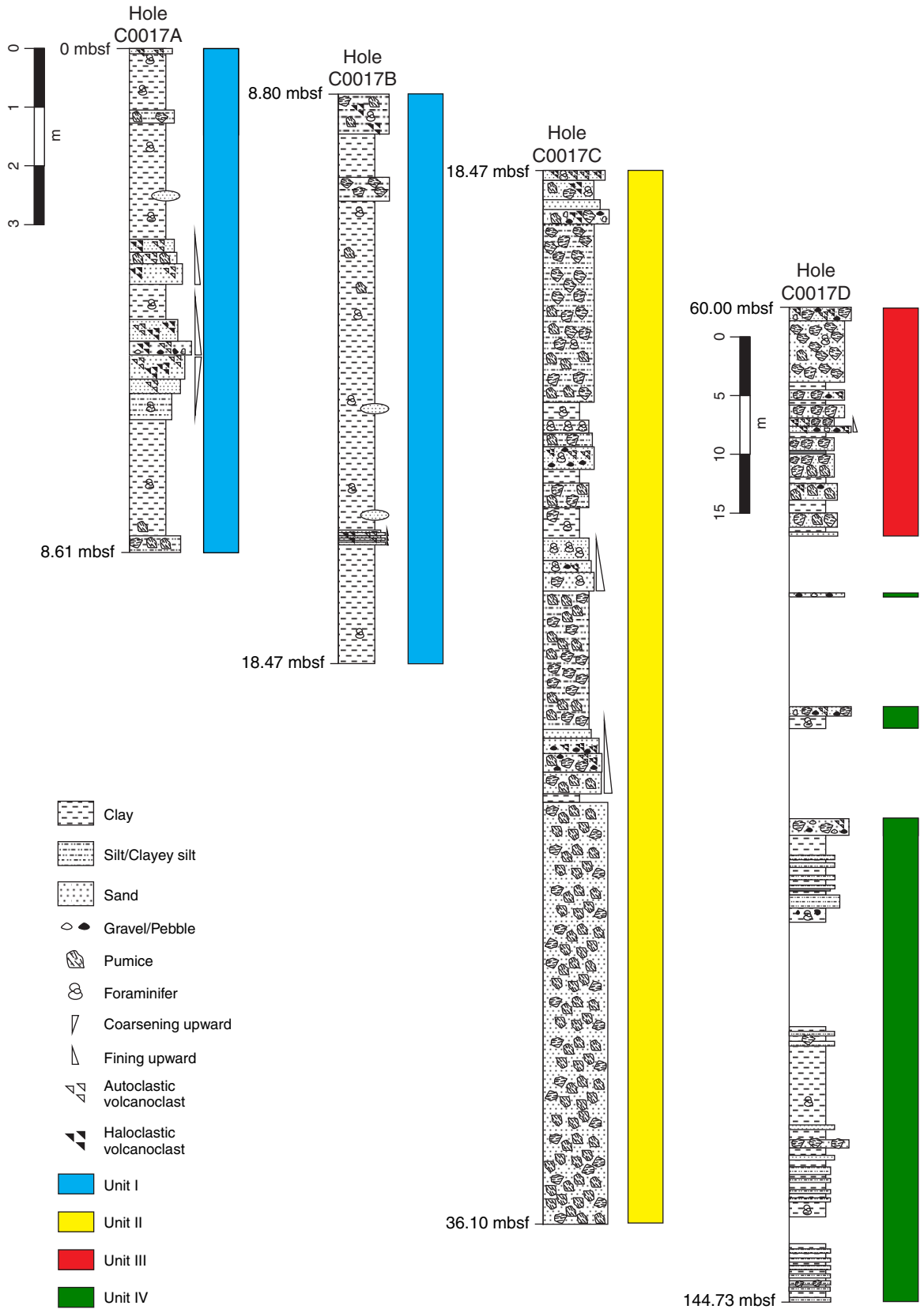

Figure F3. A. Core photograph showing contacts between interbedded sandstone and shale (interval 331-C0017A-1H-4, 78–119 cm). Note presence of rip-up mud units in overlying sand. (Continued on next page.)

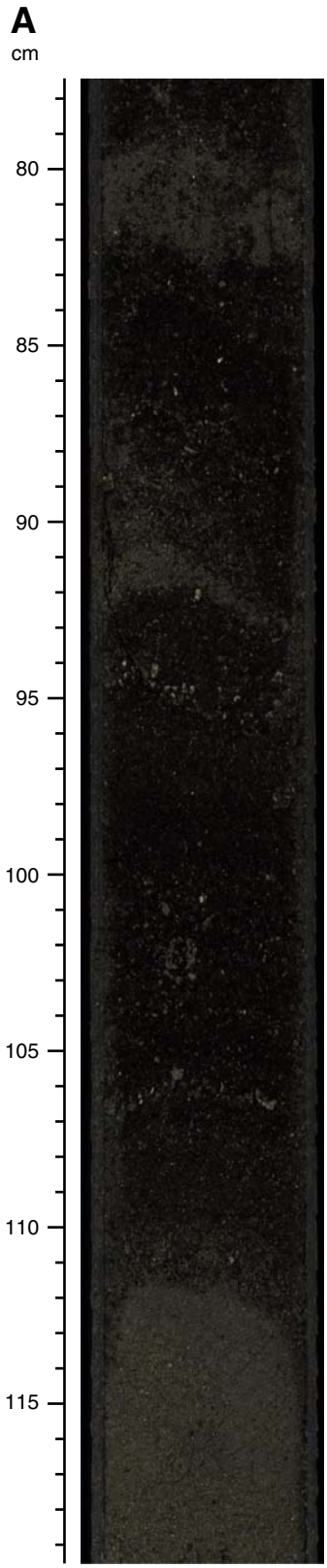

Figure F3 (continued). B. Core photograph showing sharp erosional contact between sand and mud unit at 72 cm (interval 331-C0017C-1H-4, 54–80 cm).

Figure F4. Core photograph showing intense green coloration, attributed to glauconite, on exterior of some woody pumice clasts (interval 331-C0017C-1H-2, 35–44 cm). Many other intervals had white pumice clasts with a more pervasive but less intense green coloration.

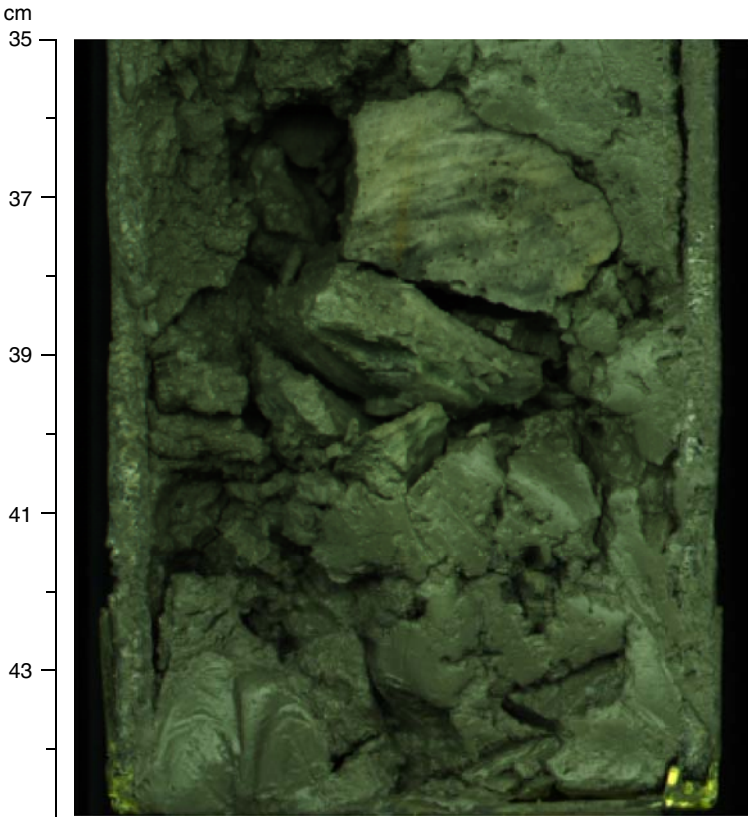

Figure F5. Series of focal scanning electron photomicrographs of a fecal pellet that has transported well-preserved coccoliths into the sediment at 10.6 mbsf, Site C0017. Note the preservation of the central area in the *Emiliania huxleyi* coccoliths (left side of F) and the bridge on the *Gephyrocapsa oceanica* (seen on the lower right side of E and F).

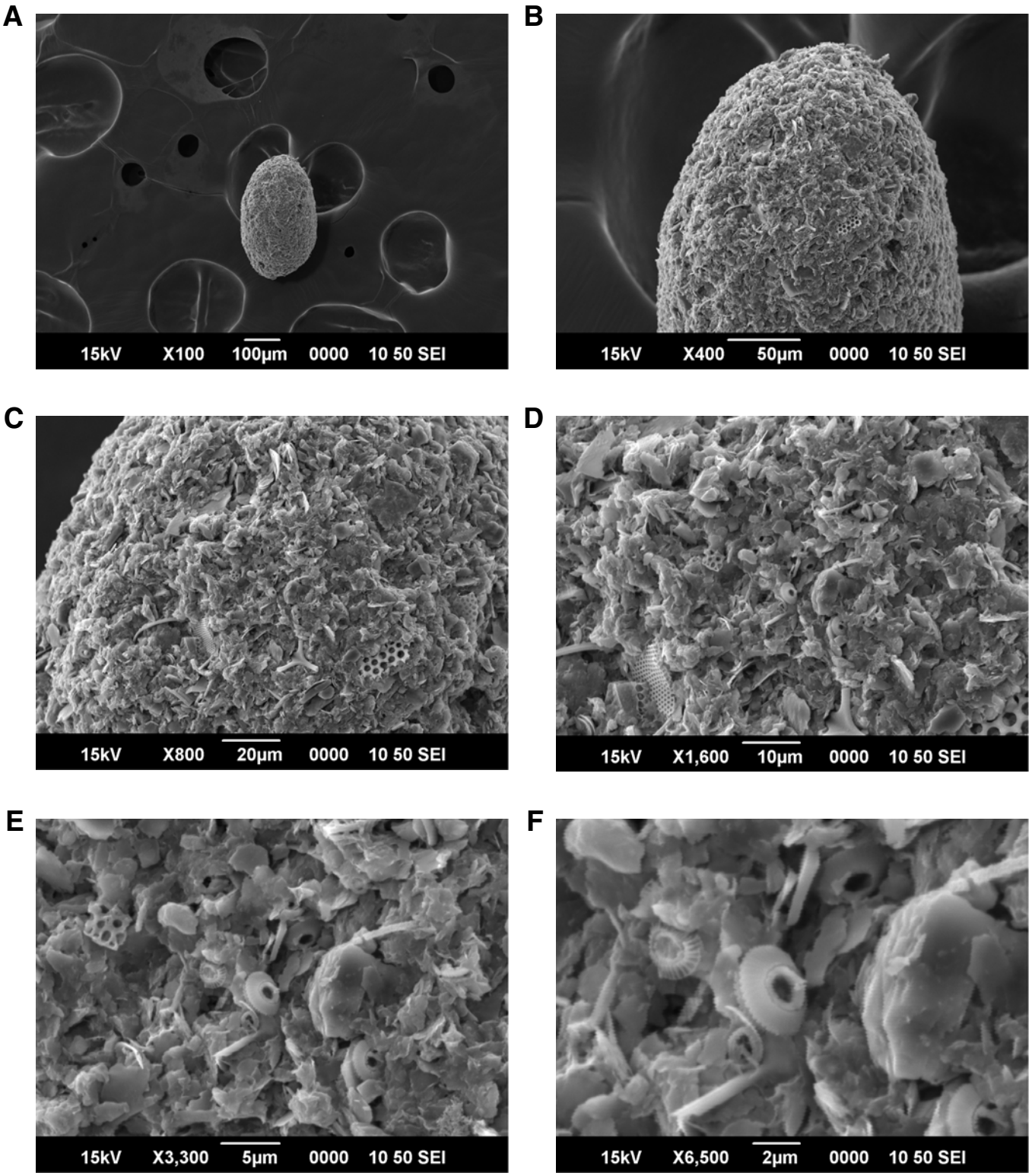

Figure F6. Core photograph showing oxidized pumiceous gravel (interval 331-C0017C-1H-7, 40–80 cm).

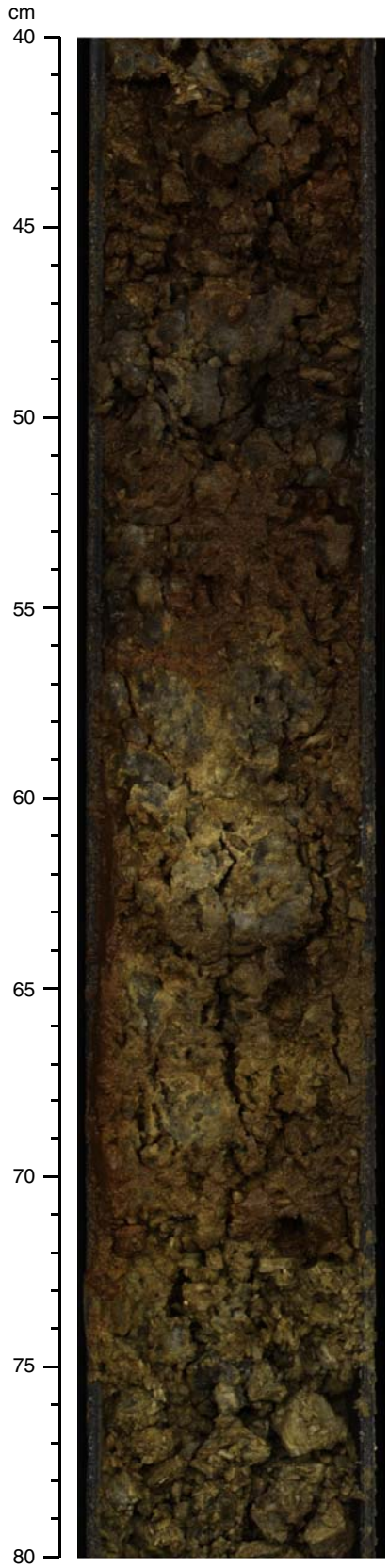

Figure F7. Core photograph showing pale, hydrothermally altered pumiceous grit intercalated with unaltered dark gray indurated clay (331-C0017D-11X-3, 40–80 cm).

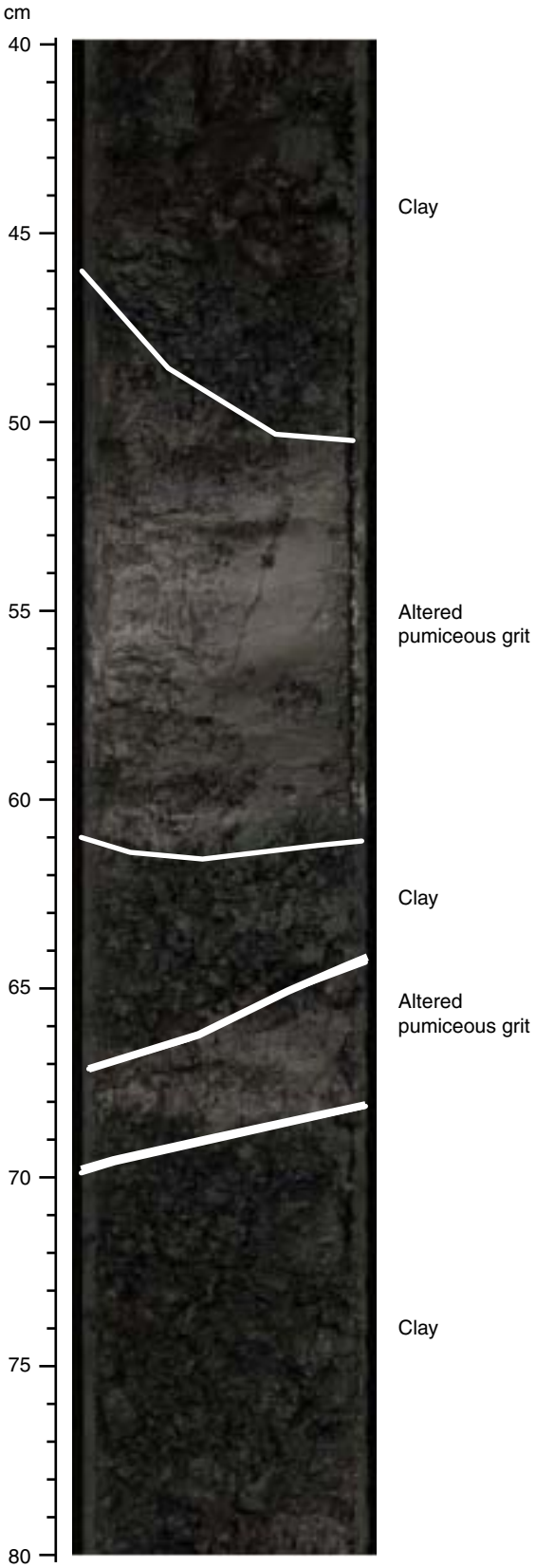

Figure F8. Plot of Na, Na/Cl, Mg, Ca, and K in pore water from Site C0017. Dashed lines indicate values in seawater as given in Table T6.

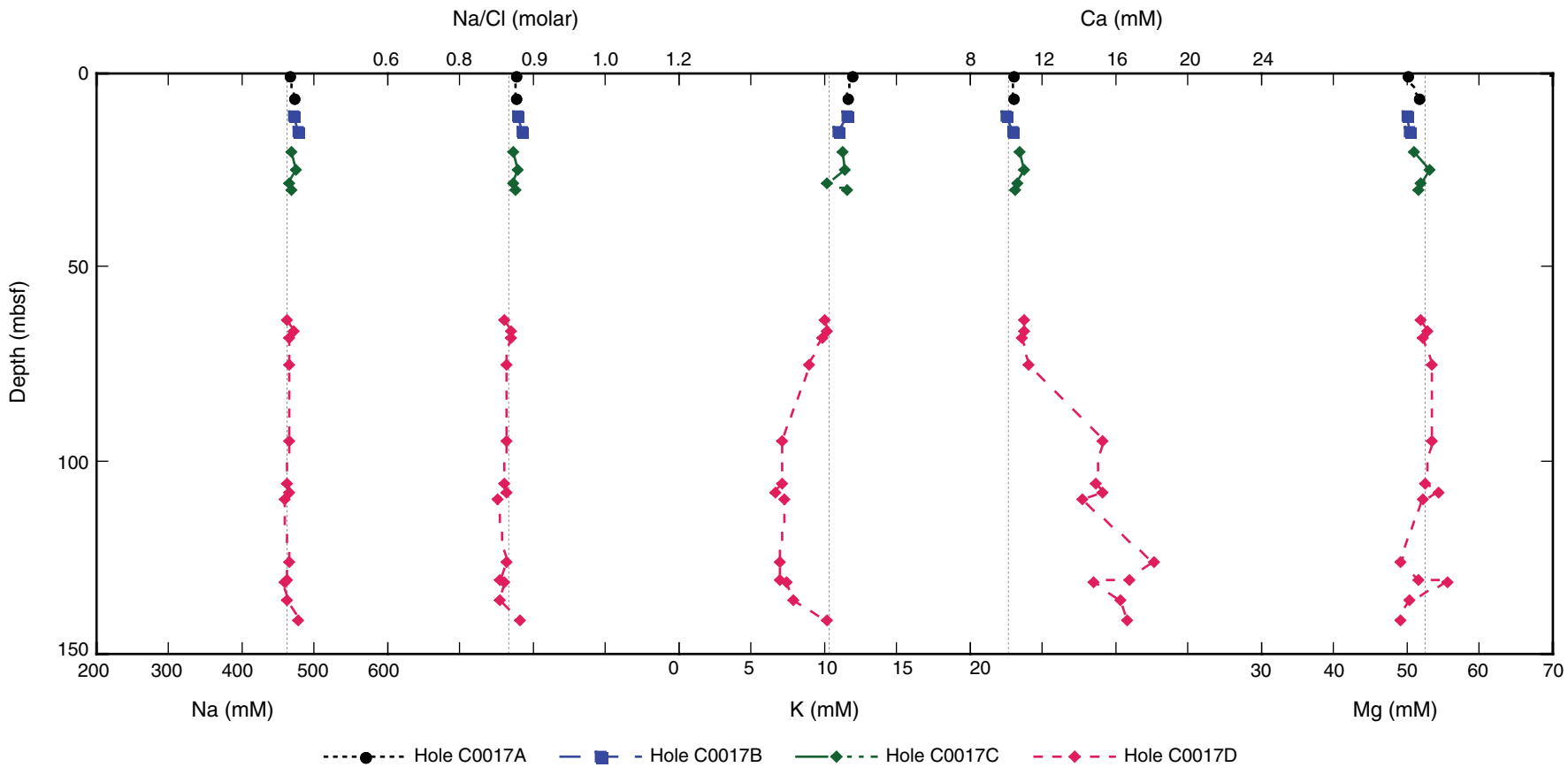

Figure F9. Plot of alkalinity, phosphate, ammonium, silicon (measured colorimetrically), and manganese in pore water from Site C0017. Note that values for ammonium that are labeled BD in Table T6 are plotted here as 0 µM.

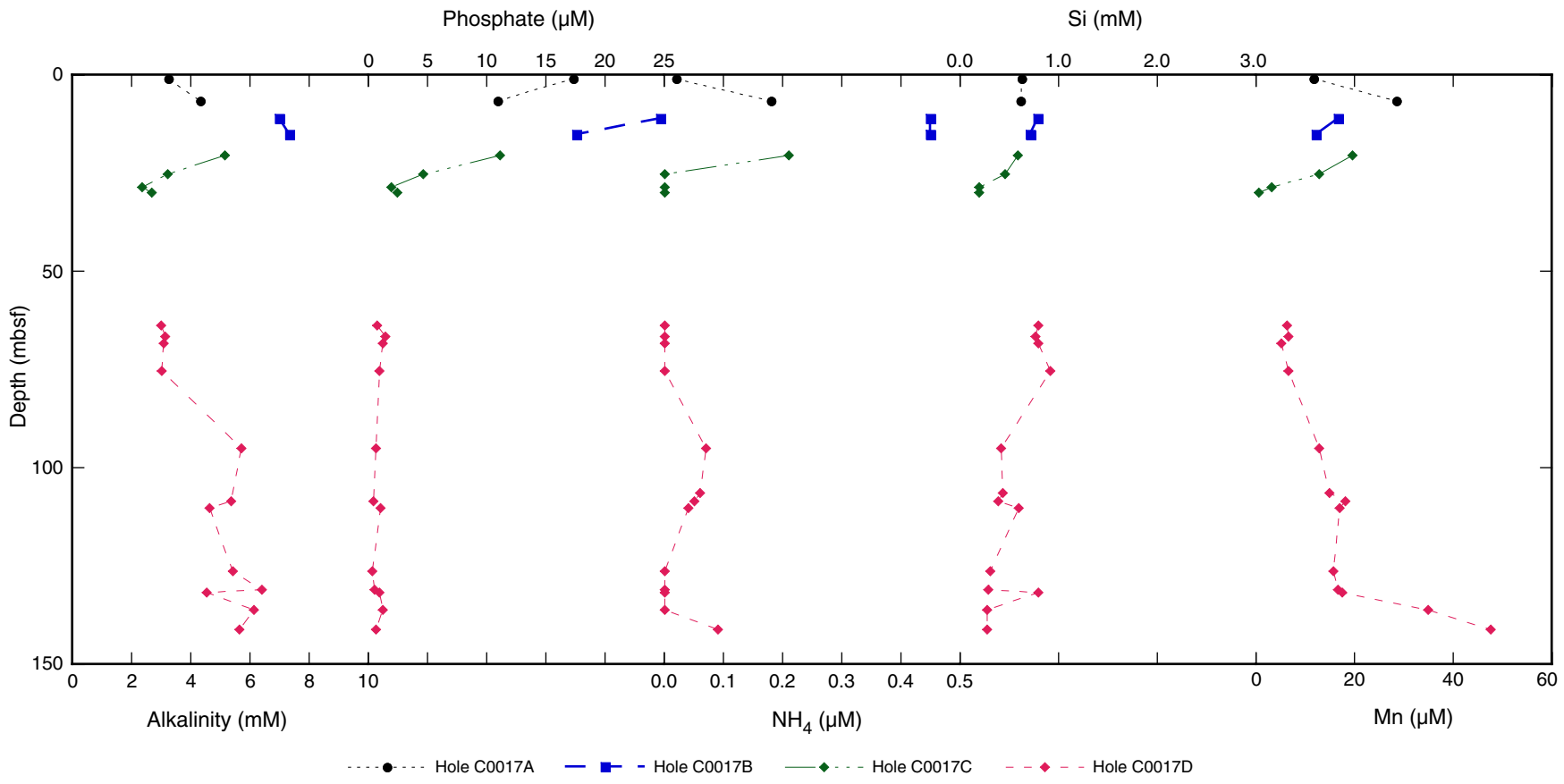

Figure F10. Plot of Cl, Br, and sulfate in pore water from Site C0017. Dashed lines indicate concentrations in seawater as given in Table T6.

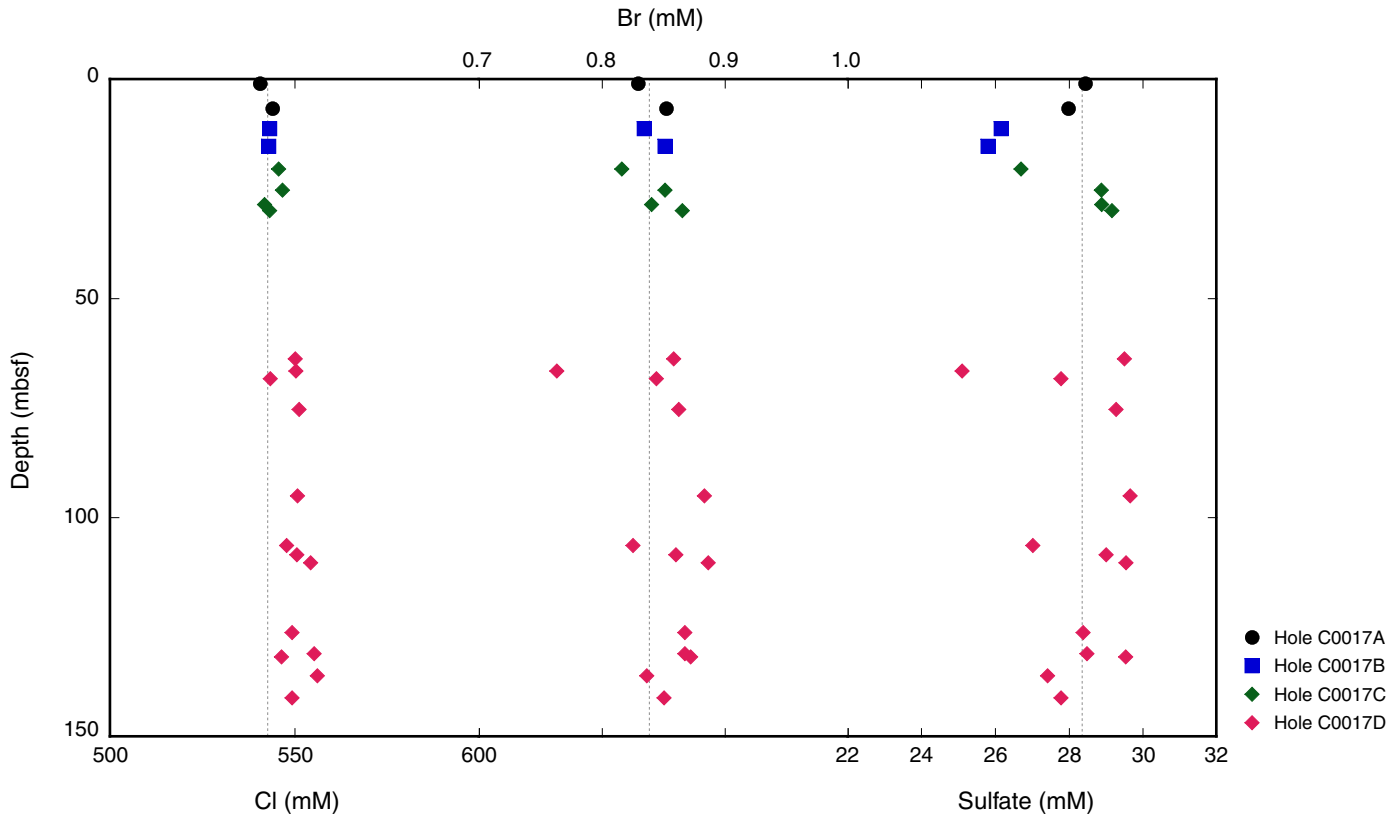

Figure F11. Plot of B, Li, and Sr in pore water from Site C0017. Dashed lines indicate concentrations in seawater as given in Table T6.

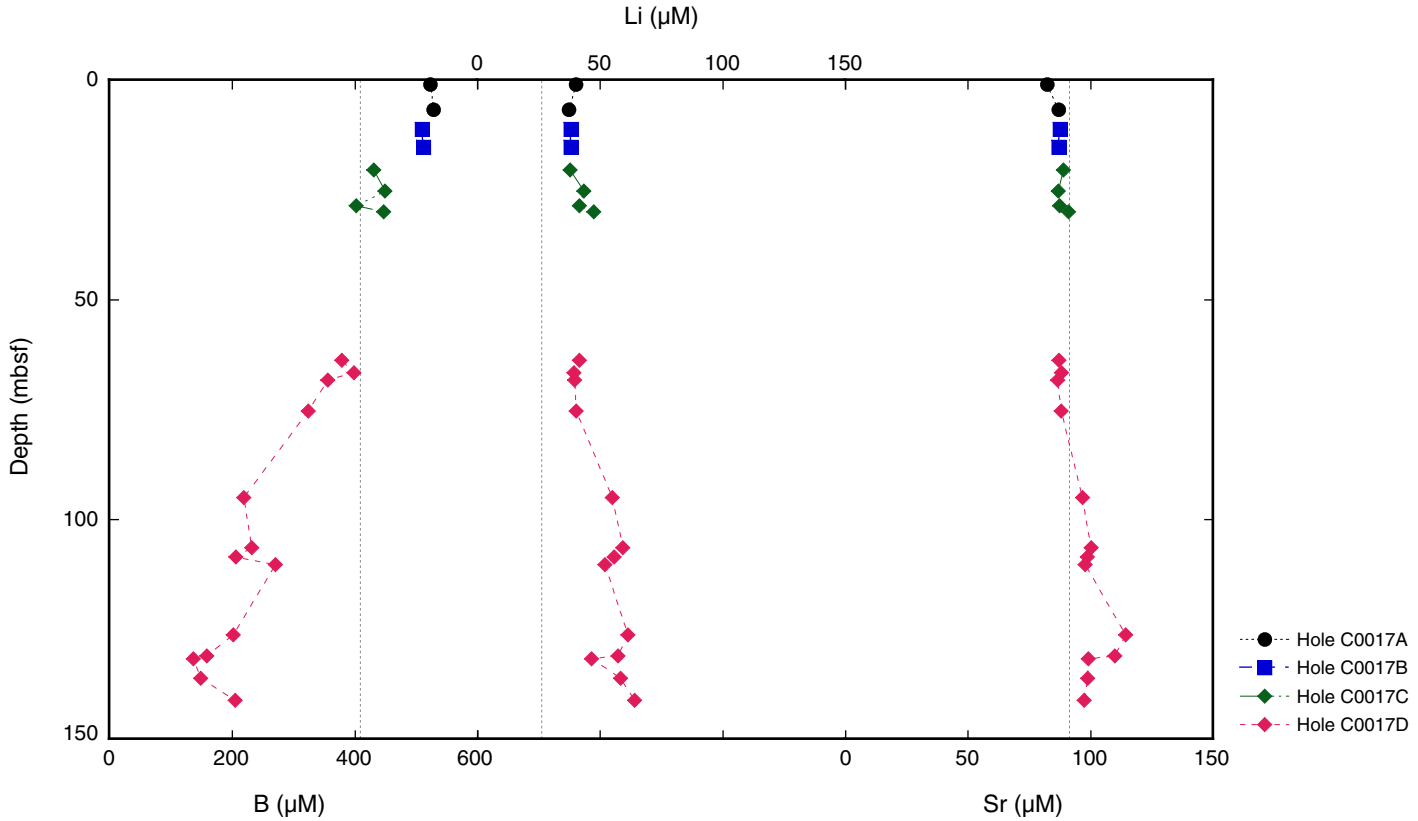

Figure F12. Plot of methane in headspace gas samples from Site C0017.

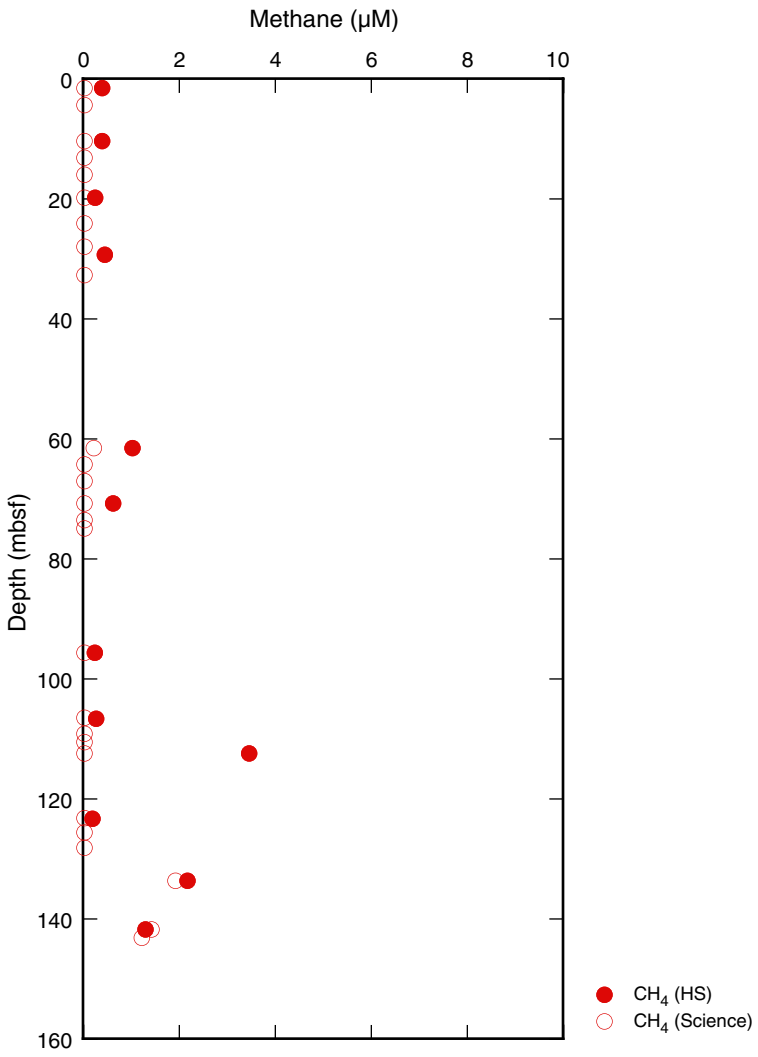

Figure F13. Plot of $CaCO_3$ in sediment from Site C0017.

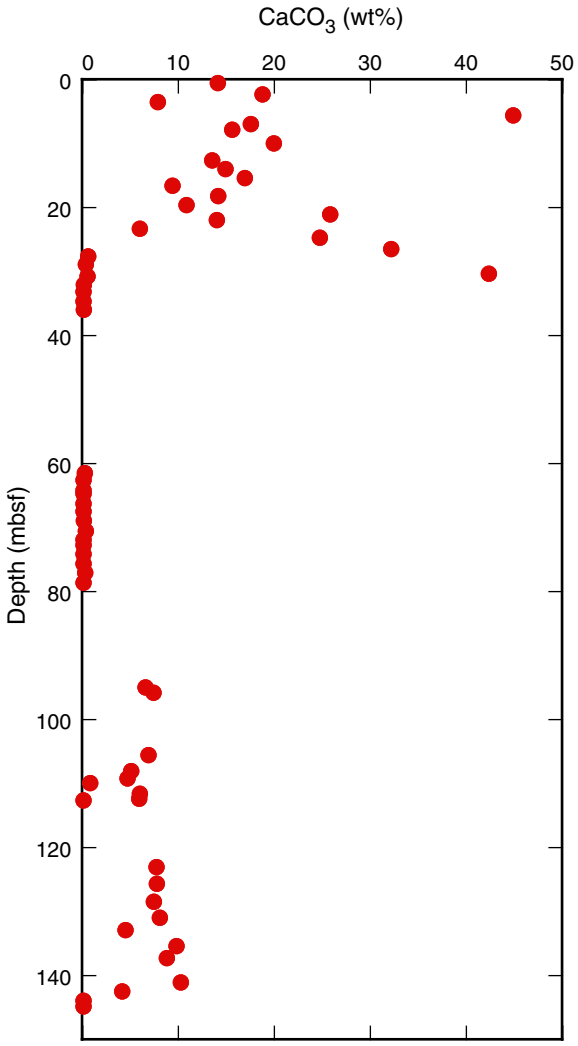

Figure F14. Plot of total organic carbon (TOC), total nitrogen (TN; logarithmic), and total sulfur (TS) in sediment from Site C0017.

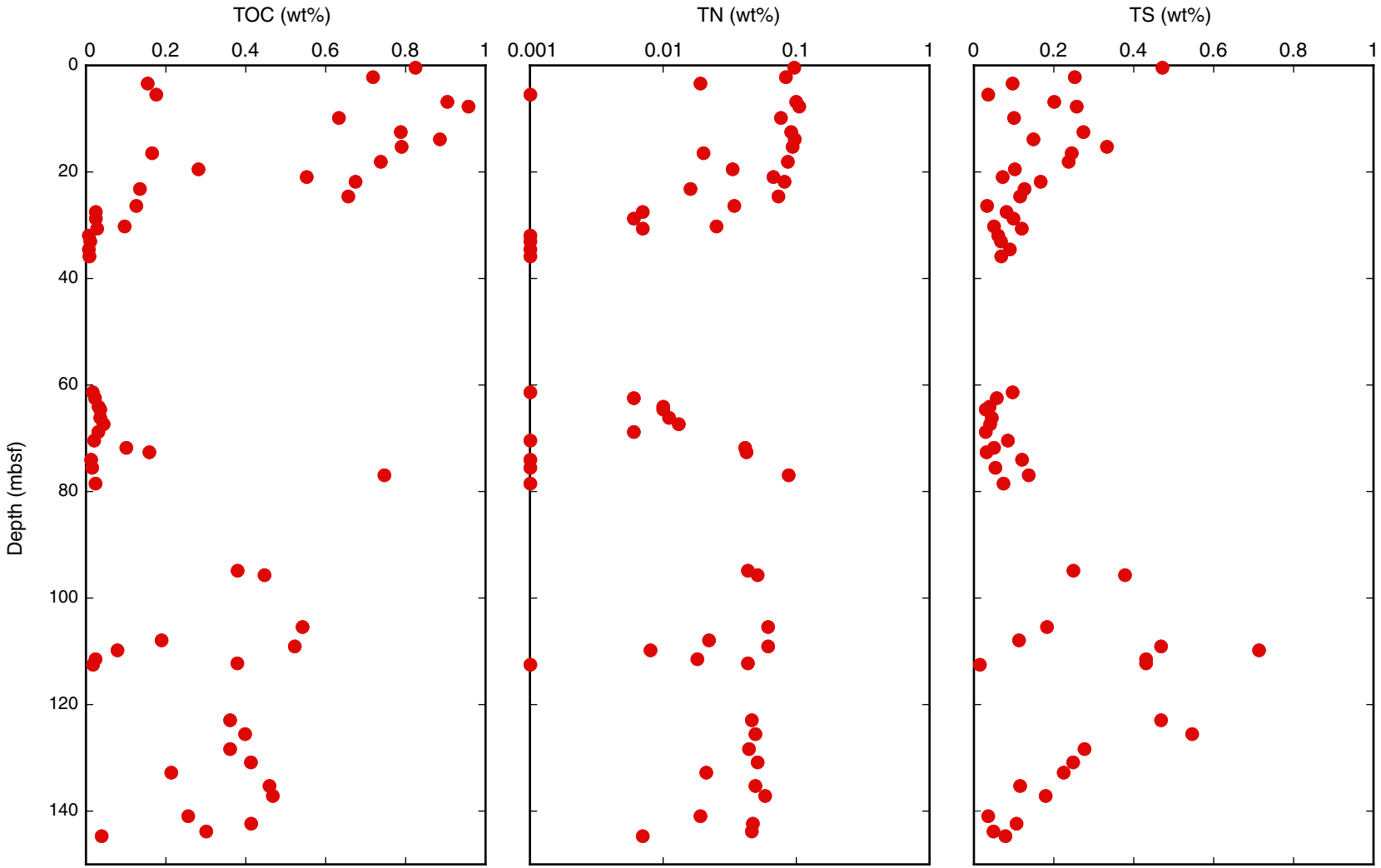

Figure F15. Plot of microbial cell counts at Site C0017. Open symbols indicate that cell counts are below our limit of detection (Expedition 331 Scientists, 2011b).

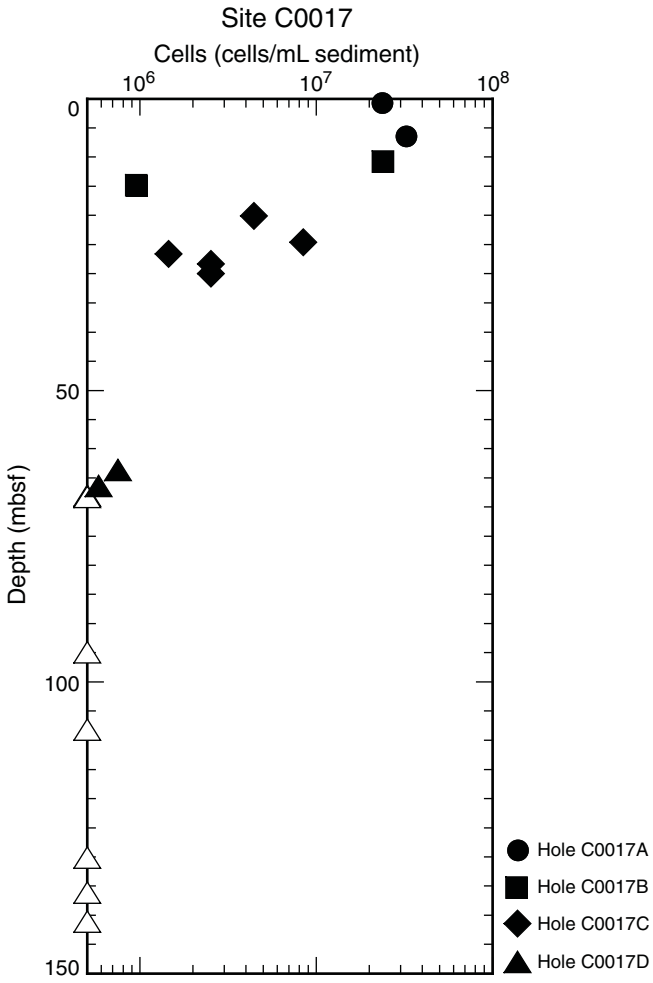

Figure F16. Paired photomicrograph images using epifluorescent (A, C, D, E, G) and phase contrast (B, D, F, H) microscopy. Arrows indicate the location of putative FeOB. **A–D.** Sample 331-C0017C-1H-6, ASW media A. **E, F.** Sample 331-C0017C-1H-7 #2, ASW media A. **G, H.** Sample 331-C0017C-2H-1, ASW media A.

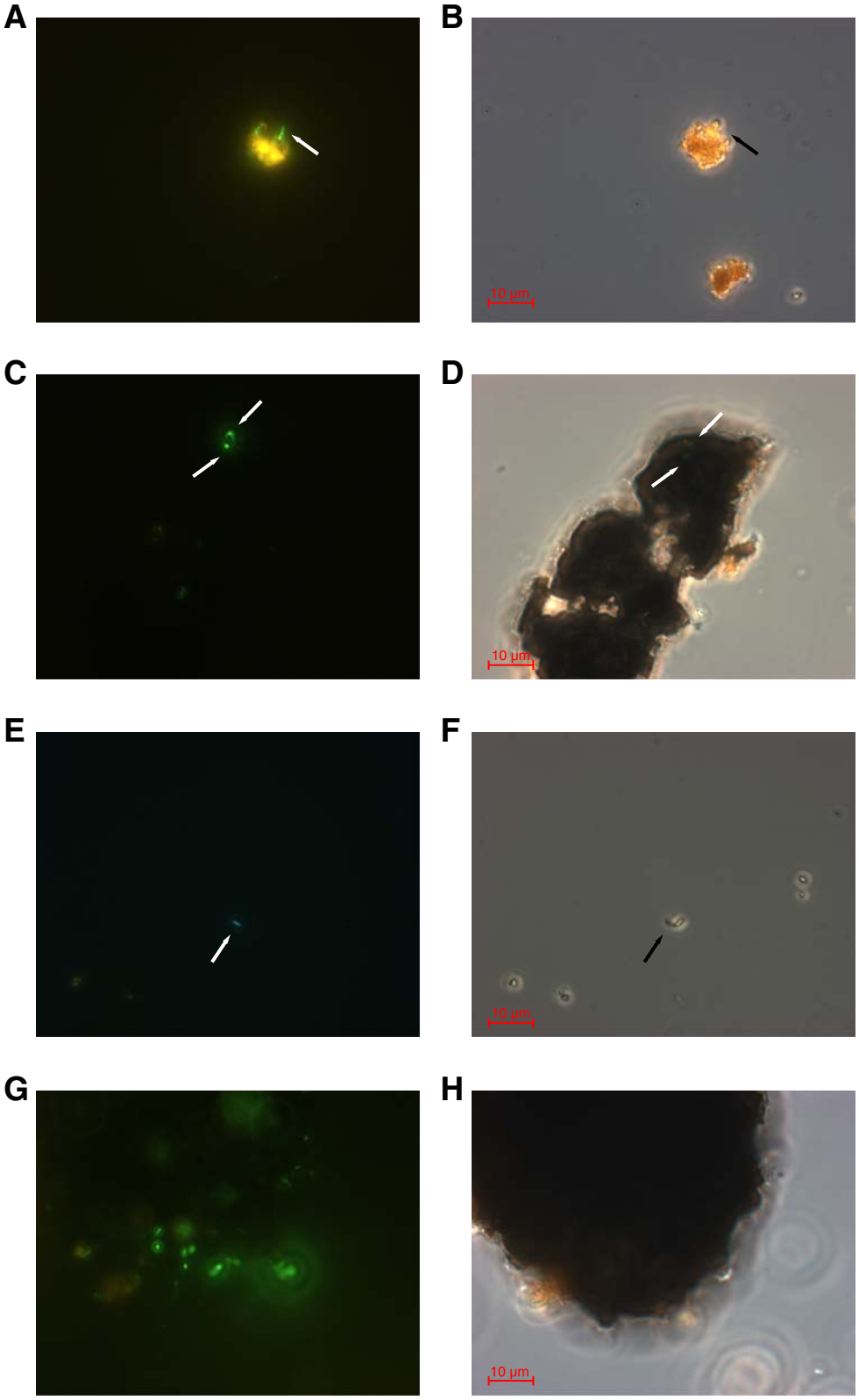

Figure F17. SEM photomicrographs with corresponding EDS spectra and quantitative analysis showing (**A**) filamentous iron and (**B**, **C**) iron oxides, possibly of biotic origin. All photomicrographs are from the original Section 331-C0017C-1H-7 before the enrichment experiments for that sample were carried out. The red circle indicates the location where the EDS spectrum was taken. cps = counts per second.

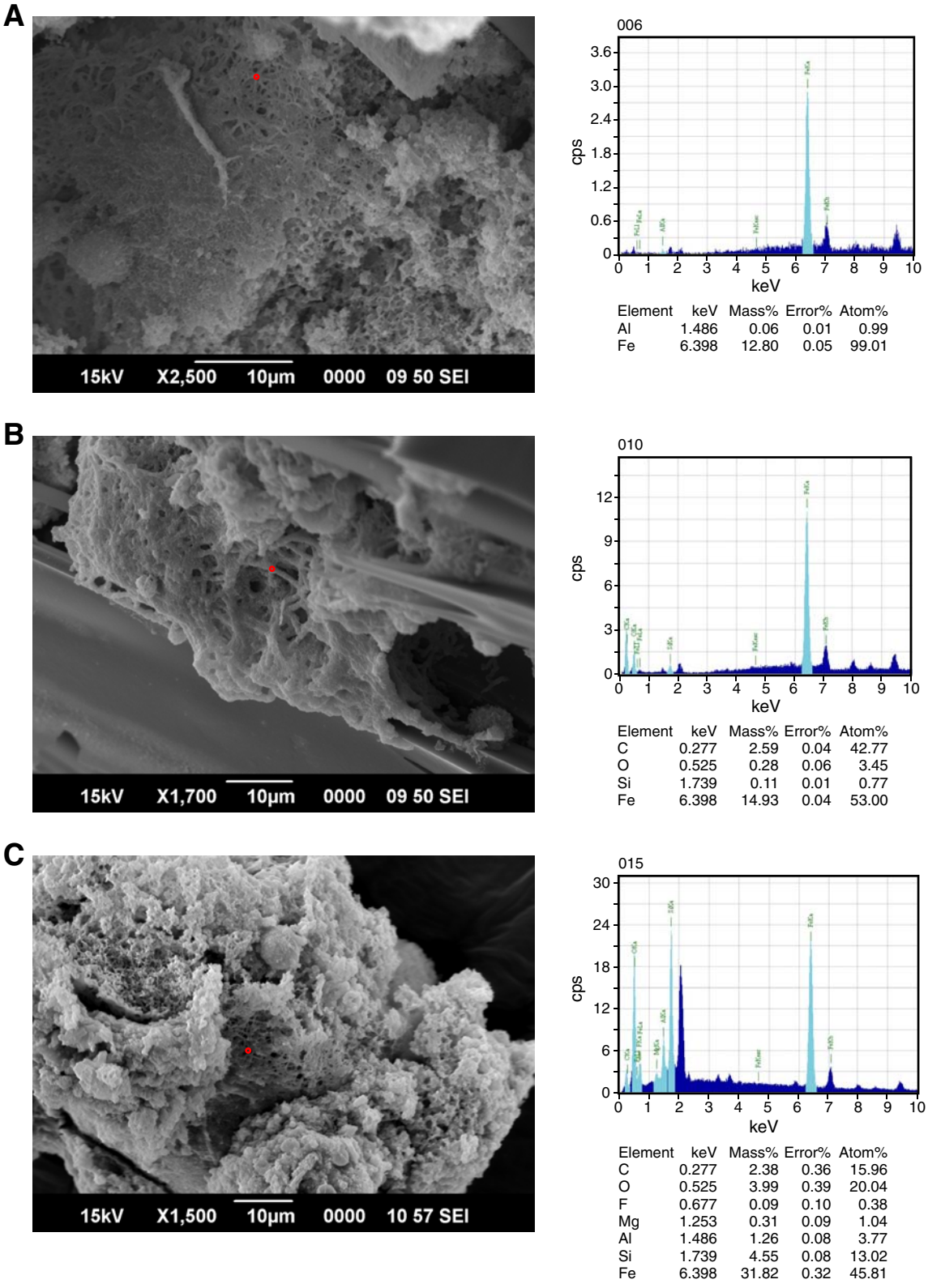

Figure F18. Plot of discrete measurements of bulk density (solid symbols) and GRA-derived bulk density (open symbols) from the multisensor logger for whole-round samples (MSCL-W), Site C0017. GRA-derived bulk density values <0 g/cm^3 are omitted for clarity.

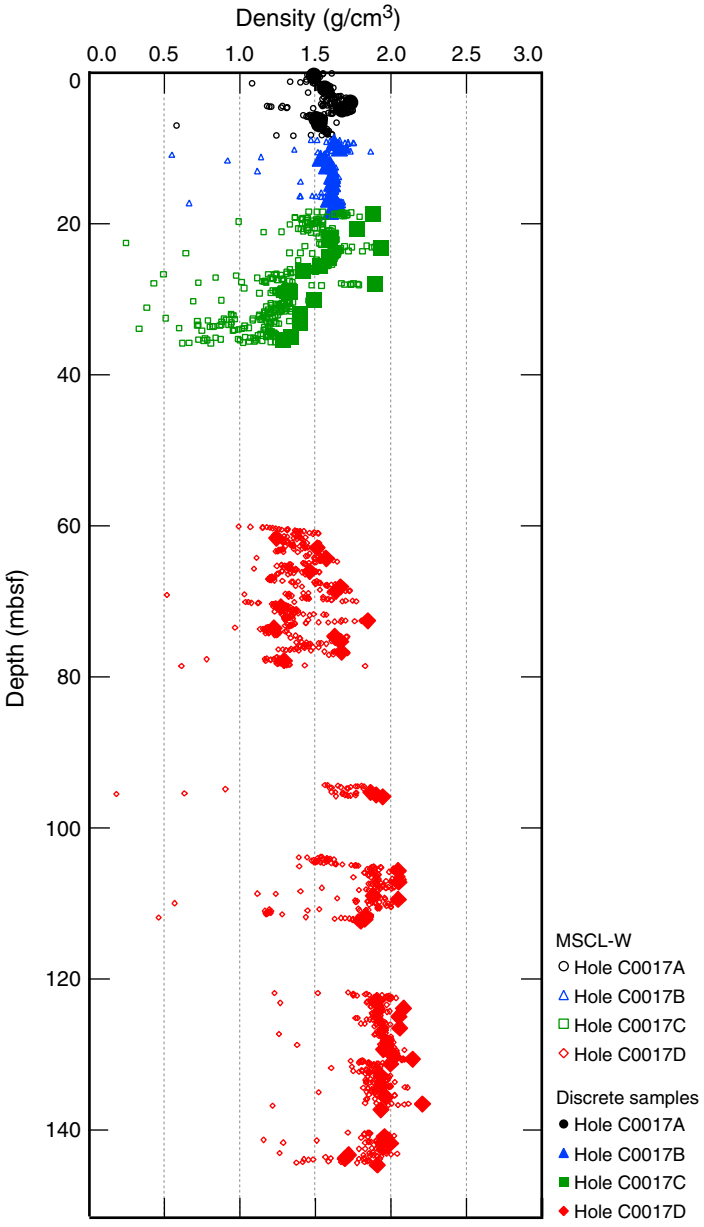

Figure F19. Plot of porosity calculated from discrete MAD measurements, Site C0017. GRA-derived bulk density values <0 g/cm^3 are omitted for clarity.

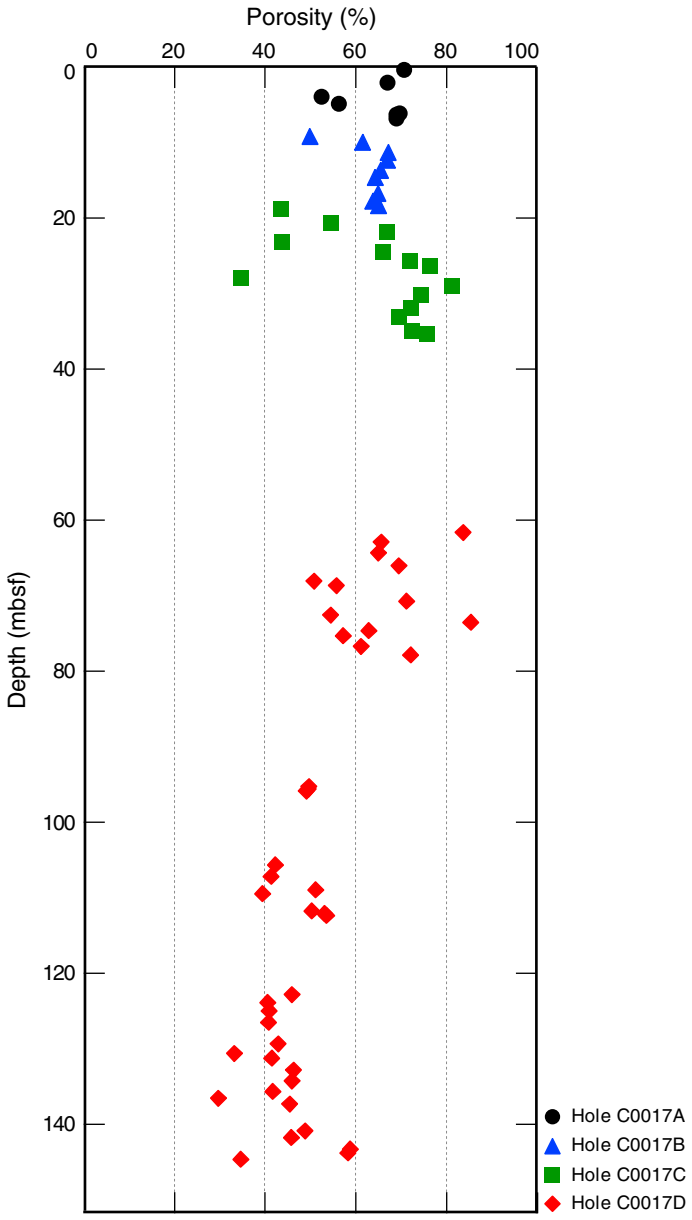

Figure F20. Plot of formation factor calculated from discrete electrical resistivity measurements, Site C0017.

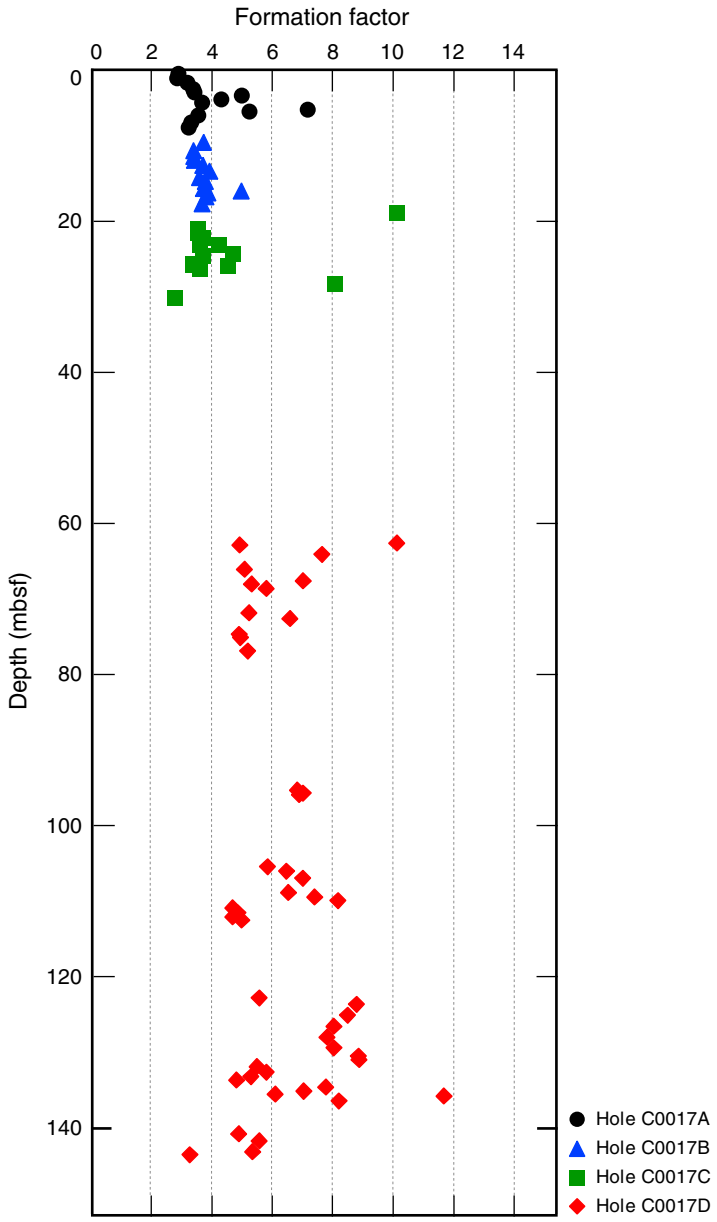

Figure F21. Plot of MSCL-derived *P*-wave velocity, Site C0017.

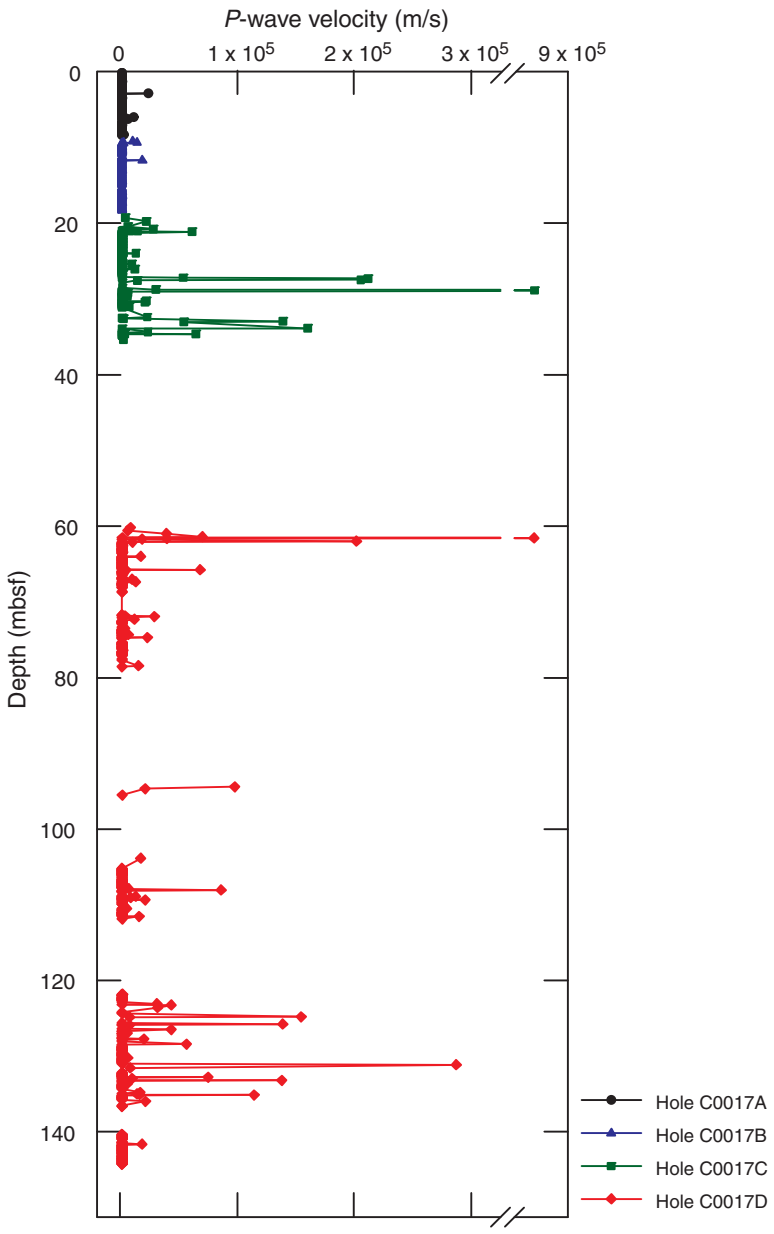

Figure F22. Plot of thermal conductivity, Site C0017.

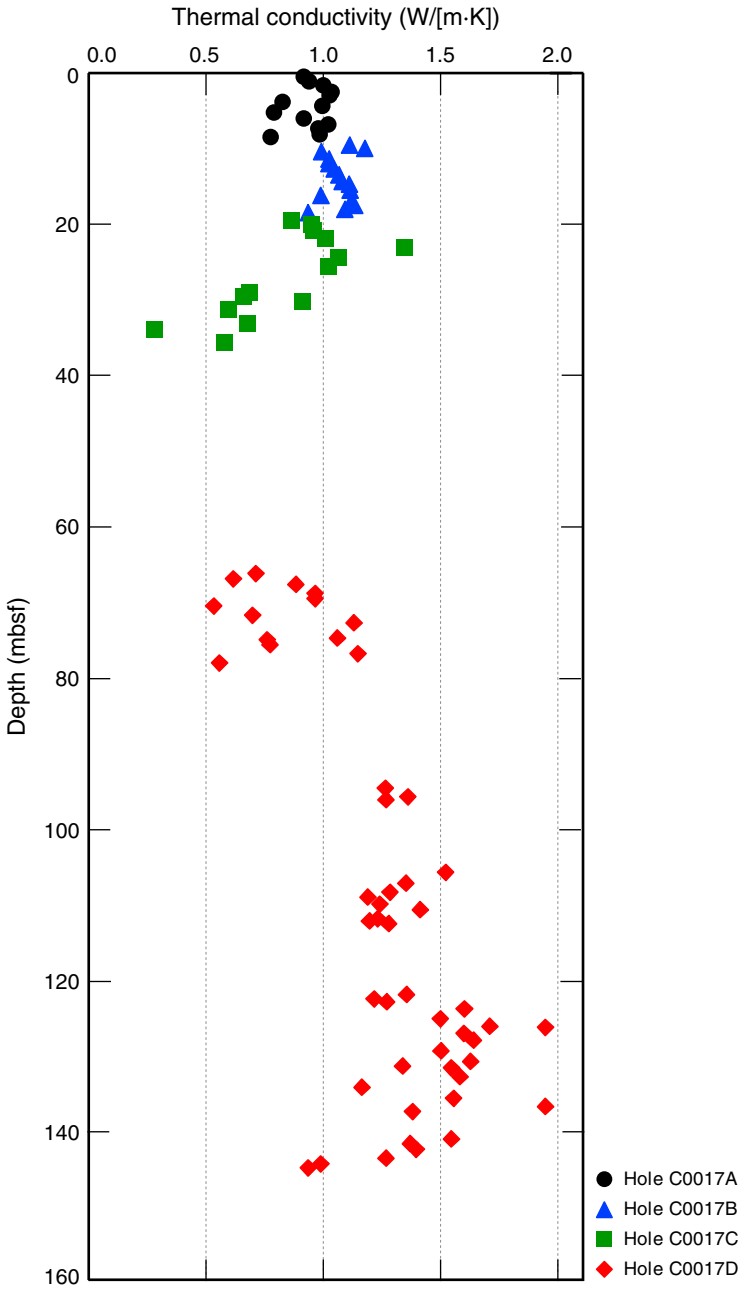

Figure F23. Plot of equilibrium temperature (red circles) and thermal conductivity, Site C0017. The point at 0 mbsf is the average bottom water temperature. Temperatures between 0 and 112 mbsf are from the APCT3 tool, and the temperature at 150.7 mbsf is derived from the thermoseal on the core barrel.

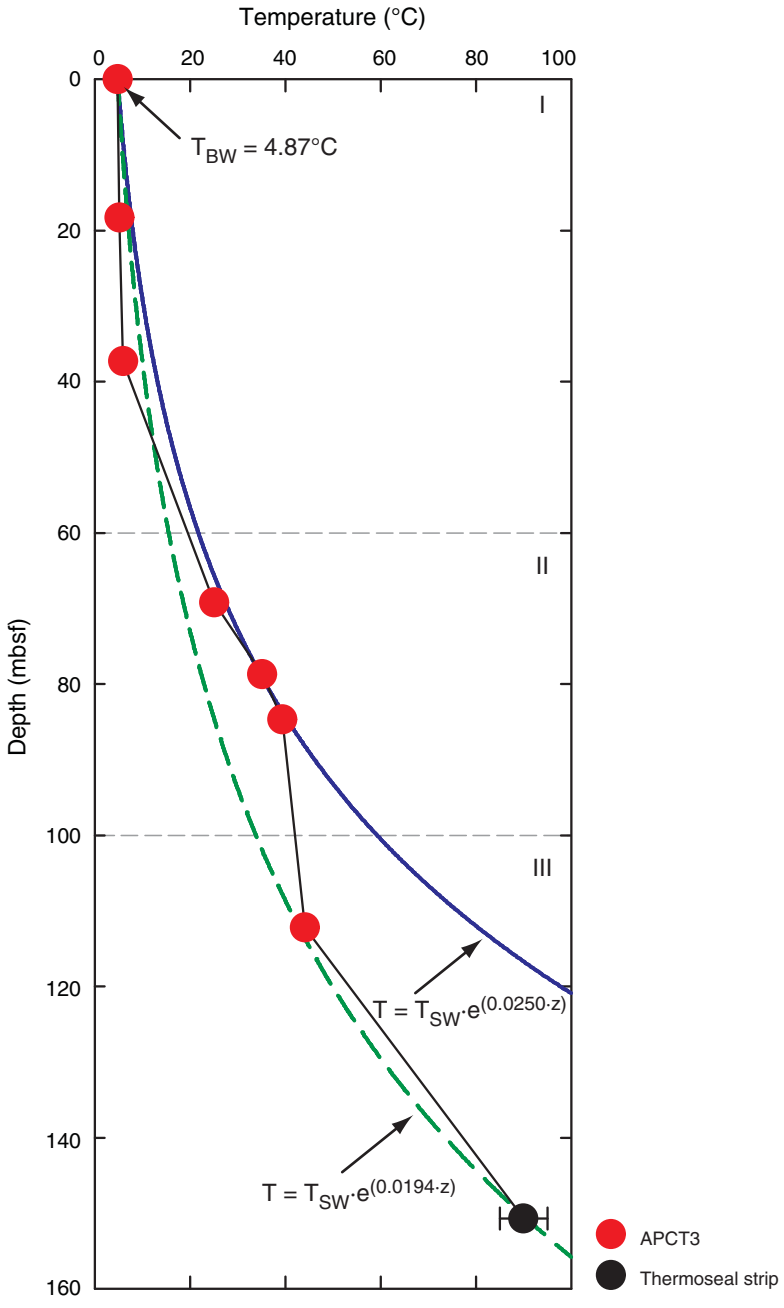

Figure F24. Temperature-time series measured during the deployment of the advanced piston corer temperature (APCT3) tool at Site C0017 (blue line). Unshaded area = data used for equilibrium temperature fit, red line = theoretical equilibrium curve, triangle = beginning of fit, inverted triangle = end of fit, dashed red line with circles = estimate of equilibrium temperature. Note frictional heating at penetration (dashed vertical line). **A.** Core 331-C0017B-1H, 18.3 mbsf. **B.** Core 331-C0017C-2H, 37.3 mbsf. **C.** Core 331-C0017D-1H, 69.2 mbsf. **D.** Core 331-C0017D-2H, 78.7 mbsf. (Continued on next page.)

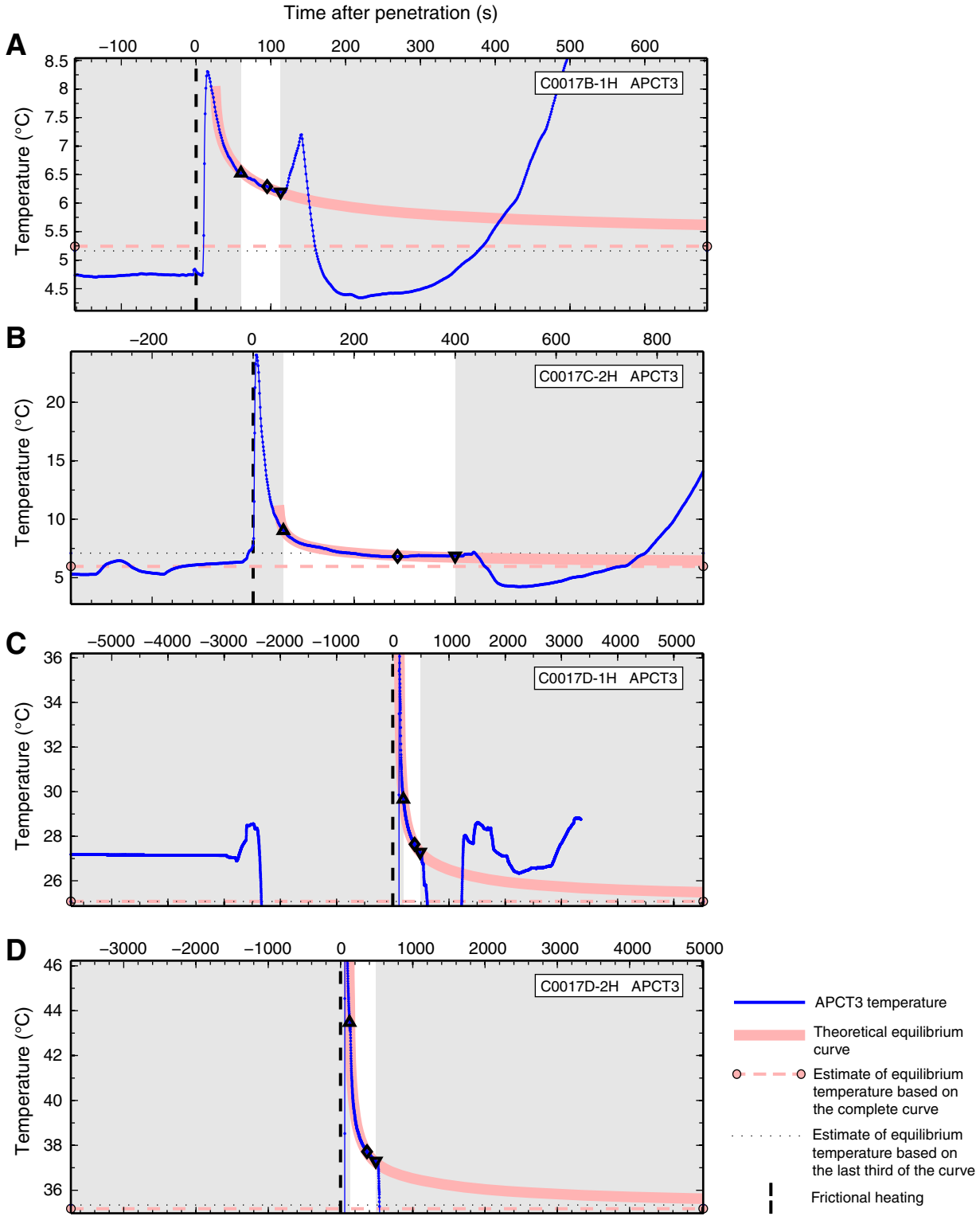

Figure F24 (continued). **E.** Core 331-C0017D-3H, 84.7 mbsf. **F.** Core 331-C0017D-4H, 84.7 mbsf. **G.** Core 331-C0017D-7H, 112.2 mbsf. **H.** Core 331-C0017D-12H, 150.7 mbsf.

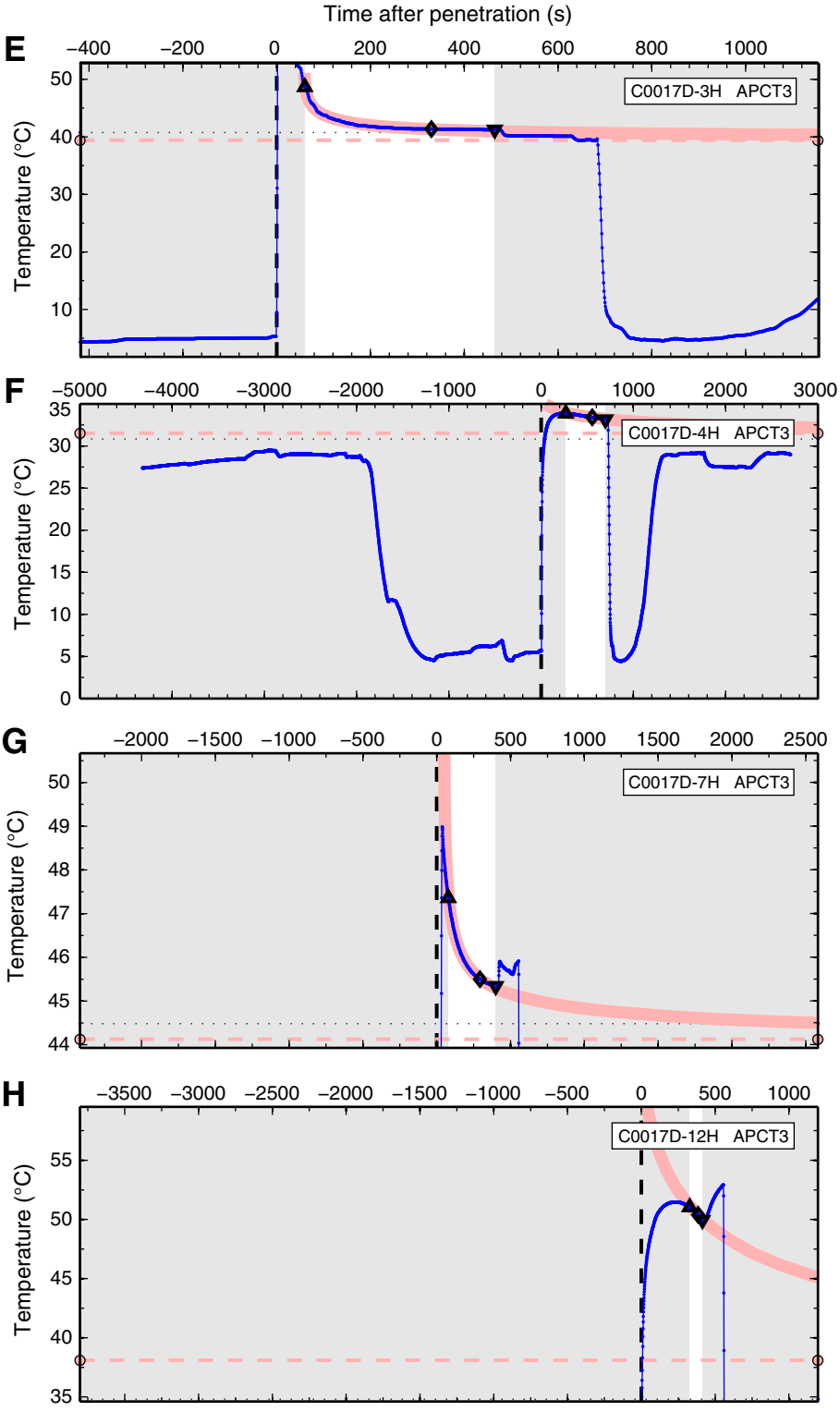

Figure F25. Plot of MSCL-W derived electrical resistivity, Site C0017.

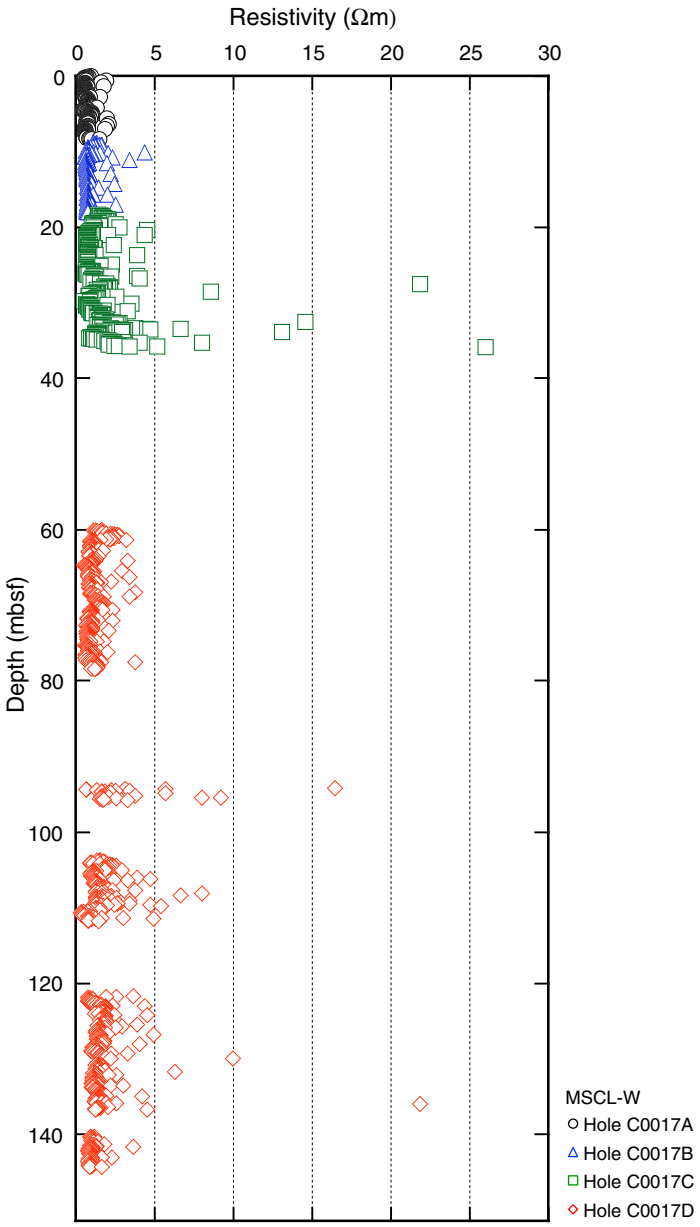

Table T1. Coring summary, Site C0017. (Continued on next page.)

Site C0017
Time on site (h): 84

Hole C0017A
Latitude: 27°47.5030′N
Longitude: 126°54.7176′E
Time on hole (h): 0.5 (1132 h, September 27–1150 h, September 27)
Seafloor depth (m DRF): 1158.1
Distance between rig floor and sea level (m): 28.5
Water depth (mbsl): 1129.6
Total depth (mDRF): 1166.9
Total penetration (mbsf): 8.8
Total length of cored section (m): 8.8
Total core recovered (m): 8.8
Core recovery: 100
Total number of cores: 1

Hole C0017B
Latitude: 27°47.5027′N
Longitude: 126°54.7176′E
Time on hole (h): 1 (1251 h, September 27–1325 h, September 27)
Seafloor depth (m DRF): 1158.1
Distance between rig floor and sea level (m): 28.5
Water depth (mbsl): 1129.6
Total depth (m DRF): 1176.4
Total penetration (mbsf): 18.3
Total length of cored section (m): 9.5
Total core recovered (m): 9.5
Core recovery: 100
Total number of cores: 1

Hole C0017C
Latitude: 27°47.5039′N
Longitude: 126°54.7202′E
Time on hole (h): 6.25 (1412 h, September 27–2040 h, September 27)
Seafloor depth (m DRF): 1158.1
Distance between rig floor and sea level (m): 28.5
Water depth (mbsl): 1129.6
Total depth (m DRF): 1208.1
Total penetration (mbsf): 50
Total length of cored section (m): 19
Total core recovered (m): 18
Core recovery: 94.7
Total number of cores: 2

Hole C0017D
Latitude: 27°47.5049′N
Longitude: 126°54.7217′E
Time on hole (h): 16.5 (0240 h, September 28–1708 h, September 28)
Seafloor depth (m DRF): 1158
Distance between rig floor and sea level (m): 28.5
Water depth (mbsl): 1129.5
Total depth (m DRF): 1307.7
Total penetration (mbsf): 150.7
Total length of cored section (m): 90.7
Total core recovered (m): 49.6
Core recovery: 54.7
Total number of cores: 12

Core	Date (2010)	Local time (h)	Depth DRF (m) Top	Depth DRF (m) Bottom	Depth (mbsf) Top	Depth (mbsf) Bottom	Advanced (m)	Recovered (m)	Recovery (%)
331-C0017A-									
1H	27 Sep	1132	1158.1	1166.9	0	8.8	8.8	8.8	100
331-C0017B-									
1H	27 Sep	1303	1166.9	1176.4	8.8	18.3	9.5	9.5	100
331-C0017C-									
1H	27 Sep	1450	1176.4	1185.9	18.3	27.8	9.5	9.5	100
2H	27 Sep	1801	1185.9	1195.4	27.8	37.3	9.5	8.5	89.5

Table T1 (continued).

Core	Date (2010)	Local time (h)	Depth DRF (m) Top	Depth DRF (m) Bottom	Depth (mbsf) Top	Depth (mbsf) Bottom	Advanced (m)	Recovered (m)	Recovery (%)
331-C0017D-									
1H	28 Sep	0628	1218	1227.2	60	69.2	9.2	9.2	100
2H	28 Sep	0915	1227.2	1236.7	69.2	78.7	9.5	9	94.7
3H	28 Sep	1205	1236.7	1242.7	78.7	84.7	6	0	0
4H	28 Sep	1423	1242.7	1242.7	84.7	84.7	0	0	0
5T	28 Sep	1720	1242.7	1252.7	84.7	94.2	9.5	0	0
6X	28 Sep	2039	1252.2	1261.7	94.2	103.7	9.5	1.8	18.9
7H	29 Sep	0042	1261.7	1270.2	103.7	112.2	8.5	8.5	100
8T	29 Sep	0248	1270.2	1279.7	112.2	121.7	9.5	0.09	0.9
9X	29 Sep	0457	1279.7	1288.7	121.7	130.7	9	9.7	107.8
10X	29 Sep	0740	1288.7	1298.2	103.7	140.2	9.5	6.5	68.4
11X	29 Sep	0944	1298.2	1307.7	140.2	149.7	9.5	4.8	50.5
12H	30 Sep	0029	1307.7	1308.7	149.7	150.7	1	0	0

DRF = drilling depth below rig floor. H = HPCS, T = EPCS, X = ESCS.

Table T2. Lithological units, Site C0017.

Lithological unit	Description	Hole, core, section, interval (cm)	Depth (mbsf) Top	Depth (mbsf) Bottom	Thickness (m)
		331-			
I	Dominantly massive hemipelagic mud, with minor pumice gravel and volcaniclastic sediment	C0017A-1H-1, 0, to 1H-CC, 21.5	0	8.635	8.635
		C0017B-1H-1, 0, to 1H-CC, 21	8.8	18.505	9.705
II	Dominantly pumiceous gravel, with minor hemipelagic mud and volcaniclastic sediment	C0017C-1H-1, 80, to 2H-CC, 28	19.1	36.17	17.07
III	Dominantly pumiceous gravel, with minor hemipelagic mud and volcaniclastic sediment	C0017D-1H-1, 115, to 2H-CC, 20	61.15	78.82	17.67
IV	Hemipelagic mud, pumice breccia, volcaniclastic sediment	C0017D-6X-1, 15, to 11X-CC, 40.5	94.35	144.745	49.7

Table T3. Interpreted results of X-ray diffraction (XRD) analyses of samples, Site C0017. (Continued on next page.)

Sample number	Core, section, interval (cm)	Lithology	Subsampled for	Result
	331-C0017A-			
35247	1H-1, 11–11.5	Dark brown volcanic glass	XRD only—check mineralogy	Glass, anorthite, augite ???
35293	1H-1, 35.5–37.5	Olive-green mud/clay	Routine chemistry	Calcite, quartz, muscovite, anorthite, chlorite
35295	1H-1, 119–120	Light gray pumice	Routine chemistry	Glass, halite, quartz
35296	1H-2, 76.5–78.5	Olive-green mud/clay	Routine chemistry	Quartz, calcite, anorthite, muscovite, chlorite
35299	1H-3, 54–56	Black volcanic sediment	Routine chemistry	Glass, calcite, quartz, albite, muscovite (trace)
35300	1H-4, 122–124	Calcareous sand	Routine chemistry	Calcite, quartz, halite, anorthite
35303	1H-5, 115–117	Olive-green mud/clay	Routine chemistry	Quartz, calcite, muscovite, chlorite, anorthite
35306	1H-6, 62–64	Olive-green mud/clay	Routine chemistry	Quartz, calcite, muscovite, anorthite, chlorite
35308	1H-CC, 16–17	Pumice	XRD only—check mineralogy	Glass, anorthite
	331-C0017B-			
35419	1H-1, 10–11	Pumice	XRD only—check mineralogy	Glass, quartz, anorthite
35420	1H-1, 103–105	Olive-green mud/clay	Routine chemistry	Quartz, calcite, muscovite, anorthite, dolomite, chlorite
35422	1H-2, 21–22	Black pumice clast	XRD only—check mineralogy	Glass, anorthite
35423	1H-3, 80–82	Olive-green mud/clay	Routine chemistry	Quartz, calcite, anorthite, muscovite, chlorite
35426	1H-4, 80–82	Olive-green mud/clay	Routine chemistry	Quartz, calcite, muscovite, anorthite, dolomite, chlorite
35428	1H-5, 80–82	Olive-green mud/clay	Routine chemistry	Quartz, calcite, anorthite, muscovite, chlorite
35429	1H-6, 57–59	Calcareous gravel, olive-green	Routine chemistry	Glass, calcite, quartz, anorthite
35432	1H-7, 80–82	Olive-green mud/clay	Routine chemistry	Quartz, calcite, muscovite, anorthite, dolomite, chlorite
	331-C0017C-			
35441	1H-1, 114–116	Olive-green mud/clay	Routine chemistry	Calcite, quartz, halite, anorthite, muscovite, chlorite (trace)
35443	1H-2, 118–120	Olive-green mud/clay	Routine chemistry	Calcite, quartz, anorthite, muscovite, chlorite
35445	1H-3, 70–72	Olive-green mud/clay	Routine chemistry	Calcite, quartz, anorthite, muscovite, chlorite, cristobalite
35447	1H-4, 64–66	Olive-green sandy clay	Routine chemistry	Quartz, anorthite, microcline, calcite, dolomite, muscovite
35449	1H-5, 60–62	Olive-green mud/clay	Routine chemistry	Quartz, calcite, anorthite, muscovite, chlorite
35451	1H-6, 97–99	Oxidized yellow-brown pumiceous clay	Routine chemistry	Calcite, quartz, muscovite, anorthite, halite, chlorite (trace)
35453	1H-7, 73–75	Oxidized yellow-brown pumiceous gravel	Routine chemistry	Glass, quartz, halite
35455	2H-1, 90–92	Oxidized yellow-brown pumiceous gravel	Routine chemistry	Glass, quartz, halite
35457	2H-2, 97–99	Oxidized yellow-brown sandy clay	Routine chemistry	Calcite, quartz, anorthite, muscovite, cristobalite, chlorite
35459	2H-3, 30–32	Oxidized yellow-brown pumiceous gravel	Routine chemistry	Glass, quartz, halite
35461	2H-4, 84–86	Pumiceous gravel	Routine chemistry	Glass, halite
35463	2H-5, 50–52	Pumiceous gravel	Routine chemistry	Glass, halite
35465	2H-6, 60–62	Pumiceous gravel	Routine chemistry	Glass, halite

Table T3 (continued).

Sample number	Core, section, interval (cm)	Lithology	Subsampled for	Result
35467	2H-7, 45–47	Pumiceous gravel	Routine chemistry	Glass, halite
	331-C0017D-			
35561	1H-1, 131–133	Gray pumiceous gravel	Routine chemistry	Glass, halite
35564	1H-2, 99–101	Pumiceous gravel with minor olive clay	Routine chemistry	Glass, quartz, halite
35565	1H-3, 121–123	Pumiceous gravel with minor olive clay	Routine chemistry	Glass, quartz, halite, anorthite
35568	1H-4, 29–31	Pumiceous gravel with olive clay	Routine chemistry	Glass, quartz, halite, anorthite
35567	1H-4, 86–87	Dark green (glauconitic?) stained pumice	XRD only—identify green stain	Glass, halite, quartz (trace)
35572	1H-5, 48–50	Pumiceous gravel with olive clay	Routine chemistry	Quartz, glass, anorthite, muscovite, halite
35575	1H-6, 26–28	Indurated pale green clay	Routine chemistry	Glass, quartz, halite, anorthite, muscovite (trace)
35576	1H-7, 30–32	Volcaniclastic sand	Routine chemistry	Quartz, anorthite, microcline, halite, muscovite
35583	2H-1, 120–122	Gray pumiceous gravel	Routine chemistry	Glass, halite, anorthite, quartz
35586	2H-2, 112–114	Light brown clay	Routine chemistry	Quartz, anorthite, muscovite, chlorite (trace)
35587	2H-3, 61–62	Mica-rich sand	XRD only	Quartz, anorthite, microcline, muscovite, brindleyite (Ni-Al silicate) ???
35588	2H-3, 52–54	Olive-green clay	Routine chemistry	Quartz, anorthite, microcline, muscovite
35591	2H-4, 51.5–53.5	Gray/Dark green pumiceous gravel	Routine chemistry	Glass, halite, anorthite, microcline
35592	2H-5, 65.5–67.5	Volcaniclastic sand	Routine chemistry	Glass, halite, anorthite
35594	2H-5, 78–79	Indurated olive-green clay	XRD only	Quartz, anorthite, muscovite, chlorite
35595	2H-6, 62–64	Dark gray indurated clay	Routine chemistry	Glass, quartz, anorthite, muscovite, halite, chlorite
35598	2H-7, 81.5–83.5	Gray pumice with green clay	Routine chemistry	Glass, anorthite, quartz, halite
35599	2H-CC, 6–7	Black volcanic glass fragment	Routine chemistry	Glass, anorthite
35651	6X-1, 63–65	Brown clay–fizzes with HCl	Routine chemistry	Quartz, anorthite, dolomite, microcline, muscovite, chlorite
35653	6X-2, 16–18	Brown clay–fizzes with HCl	Routine chemistry	Quartz, anorthite, calcite, muscovite, chlorite
35694	7H-2, 30–32	Gray indurated calcareous clay	Routine chemistry	Quartz, anorthite, calcite, microcline, muscovite, chlorite
35696	7H-3, 134–136	Silt with gray calcareous clay	Routine chemistry	Quartz, anorthite, calcite, microcline, muscovite, chlorite, tremolite ???
35698	7H-4, 110–112	Gray indurated calcareous clay	Routine chemistry	Quartz, anorthite, microcline, muscovite, chlorite
35700	7H-5, 42–44	Brown volcaniclastic silt	Routine chemistry	Glass, quartz, anorthite, pyrite
35702	7H-6, 66–68	Slightly soupy gray calcareous clay	Routine chemistry	Quartz, anorthite, calcite, microcline, dolomite, muscovite, chlorite
35706	7H-CC, 22–24	Gray indurated calcareous clay and silt	Routine chemistry	Quartz, anorthite, microcline, muscovite, chlorite
35704	8T-CC, 0–2	Redrill–flow-banded welded tuff	Routine chemistry	Glass, anorthite, microcline
35731	9X-2, 110–112	Gray indurated calcareous clay	Routine chemistry	Quartz, anorthite, calcite, microcline, muscovite, chlorite
35733	9X-4, 100–102	Gray indurated calcareous clay	Routine chemistry	Quartz, anorthite, calcite, microcline, dolomite, muscovite, chlorite
35735	9X-6, 100–102	Gray indurated calcareous clay	Routine chemistry	Quartz, anorthite, calcite, microcline, muscovite, chlorite
35737	9X-8, 70–72	Gray indurated calcareous clay	Routine chemistry	Quartz, anorthite, calcite, microcline, muscovite, chlorite
35739	9X-CC, 40–42	Dark brown sugary pumice	XRD only	Glass, quartz, anorthite, pyrite
35780	10X-2, 60–62	Dark gray calcareous clayey silt	Routine chemistry	Quartz, anorthite, dolomite, microcline, muscovite, chlorite
35782	10X-4, 32–34	Gray indurated calcareous clay	Routine chemistry	Quartz, anorthite, calcite, microcline, dolomite, muscovite, chlorite
35784	10X-CC, 40–42	Gray indurated calcareous clay	Routine chemistry	Quartz, anorthite, calcite, microcline, muscovite, chlorite
35892	11X-1, 70–72	Brown calcareous clay	Routine chemistry	Quartz, anorthite, calcite, microcline, dolomite, muscovite, chlorite
35894	11X-2, 68–70	Brown calcareous clay	Routine chemistry	Quartz, anorthite, dolomite, microcline, muscovite, chlorite
35898	11X-3, 27–29	White-gray hydrothermal? grit	XRD only	Glass, halite, quartz, sylvite
35896	11X-3, 75–77	Brown calcareous clay	Routine chemistry	Quartz, anorthite, muscovite, chlorite
35900	11X-CC, 33–35	White-gray hydrothermal? grit	Routine chemistry	Glass, quartz, anorthite

Phases listed in approximate order of decreasing abundance.

Table T4. Dry mass and light microscopic observations of micropaleontology samples, Site C0017.

Core, section, interval (cm)	Depth (mbsf)	Mass (g)			Comments
		>1 mm	150 µm to 1 mm	63–150 µm	
331-C0017A-					
1H-CC, 20–21	8.63	16.22	0.59	0.56	Foraminifers—pumice clasts and fragments
331-C0017B-					
1H-2, 38–40	10.59	NM	NM	NM	Foraminifers—pumice fragments, fecal pellets, large <63 µm fraction
1H-CC, 20–21	18.50	0.29	1.06	0.7	Foraminifers—pumice fragments, large <63 µm fraction
331-C0017C-					
1H-CC, 29.5–30.5	28.17	14.37	1.42	0.53	Pumice clasts and fragments >> foraminifers
2H-CC, 30–31	36.16	6.25	2.6	1.14	Pumice clasts and fragments
331-C0017D-					
1H-CC, 26.5–27.5	69.41	5.53	3.95	1.47	Pumice clasts and fragments
2H-CC, 19.5–20.5	78.82	10.11	6.71	2.77	Pumice clasts and fragments
3H-CC, 0–0.5	78.70	0.57	1.75	0.85	Pumice clasts and fragments, a small core catcher sample
4H		—	—	—	No core
5H		—	—	—	No core
6X-CC, 32–33	96.12	0.62	1.06	3.51	Pumice > foraminifers, large <63 µm fraction
7H-CC, 44.5–45.5	112.65	0.24	0.53	3.2	Foraminifers-pumice with pyrite >> framboidal pyrite, large <63 µm fraction
8T		—	—	—	No PAL sample (1 cm core)
9X-CC, 33–34	131.55	0.29	0.27	1.32	Few foraminifers, pumice with pyrite, large <63 µm fraction
9X-CC, 45–46	131.67	8.99	12.85	4.32	Pumice clasts and fragments; not representative of core (mud); resampled
10X-CC, 77–78	137.49	0.08	BD	0.3	Few foraminifers, pumice with pyrite, large <63 µm fraction
11X-CC, 39.5–40.5	144.74	3.67	5.83	2.48	Pumice clasts and fragments

NM = not measured. — = no data. BD = below detection. PAL = paleontology.

Table T5. Foraminifers: micropaleontological observations, Site C0017. This table is available in an **oversized format.**

Table T6. Chemical composition of interstitial pore water, Site C0017. (Continued on next page.)

Core, section, interval (cm)	Depth (mbsf)	Volume (mL)	Refractive index	pH	Alkalinity (mM)	Cl (mM)	Phosphate (μM)	NH_4 (mM)	Si (mM)*	Br (mM)	SO_4 (mM)	Na (mM)	Na_{charge}	Difference (%)	Na/Cl	K (mM)	Mg (mM)
331-C0017A-																	
1H-1, 80–90	0.80	36.0	1.33936	7.5	3.237	540.5	17.3	0.02	0.62	0.829	28.43	466	469	0.62	0.862	11.8	50.1
1H-5, 88–98	6.52	40.5	1.33935	7.5	4.313	543.9	10.9	0.18	0.61	0.852	27.97	471	470	0.22	0.865	11.6	51.5
331-C0017B-																	
1H-2, 85–95	11.06	53.0	1.33934	7.47	6.993	543.1	24.7	0.45	0.79	0.834	26.15	471	471	0.08	0.867	11.5	50.1
1H-5, 70–80	15.14	57.0	1.33934	7.56	7.340	542.9	17.6	0.45	0.71	0.851	25.79	477	470	1.41	0.878	11.0	50.4
331-C0017C-																	
1H-2, 60–70	20.31	58.0	1.33934	7.34	5.136	545.5	11.1	0.21	0.58	0.816	26.68	468	470	0.45	0.858	11.2	50.9
1H-5, 115–125	25.09	59.0	1.33936	7.41	3.205	546.6	4.6	BD	0.45	0.851	28.86	474	469	1.06	0.867	11.4	53.0
2H-1, 65–75	28.45	58.0	1.33930	7.68	2.340	541.7	1.9	BD	0.19	0.840	28.87	465	467	0.59	0.858	10.2	51.9
2H-2, 65–75	29.85	55.0	1.33935	7.41	2.668	543.1	2.4	BD	0.19	0.865	29.15	468	469	0.25	0.862	11.5	51.7
331-C0017D-																	
1H-3, 80–90	63.62	32.5	1.33936	7.27	2.984	550.1	0.7	BD	0.79	0.858	29.49	462	478	3.24	0.840	10.0	51.8
1H-5. 80–90	66.44	28.5	1.33937	7.36	3.118	550.2	1.4	BD	0.76	0.763	25.09	470	466	0.83	0.855	10.2	52.8
1H-6, 110–120	68.15	30.5	1.33936	7.45	3.064	543.3	1.2	BD	0.79	0.844	27.77	465	467	0.44	0.856	9.8	52.2
2H-5, 30–40	75.15	37.5	1.33935	7.43	3.001	551.1	0.9	BD	0.91	0.862	29.26	465	475	2.08	0.844	8.9	53.5
6X-1, 66–76	94.86	19.5	1.33941	7.78	5.694	550.7	0.6	0.07	0.41	0.883	29.65	464	472	1.68	0.843	7.1	53.5
7H-2, 112–122	106.23	16.5	1.33940	—	—	547.7	—	0.06	0.43	0.825	27.01	461	460	0.23	0.842	7.1	52.6
7H-4, 42–52	108.34	14.3	1.33941	7.67	5.346	550.5	0.4	0.05	0.38	0.860	28.99	465	469	0.83	0.845	6.6	54.3
7H-5, 80–90	110.14	24.5	1.33941	7.4	4.618	554.2	1.0	0.04	0.59	0.886	29.53	459	479	4.15	0.828	7.2	52.2
9X-5, 25–35	126.13	25.5	—	7.44	5.409	549.2	0.3	BD	0.30	0.867	28.37	464	471	1.49	0.844	7.0	49.1
9X-8, 75–90	130.86	14.0	1.33954	7.88	6.390	555.2	0.5	BD	0.28	0.867	28.48	461	476	3.07	0.830	7.0	51.6
10X-1, 88–102	131.58	11.5	—	7.77	4.524	546.3	0.9	BD	0.79	0.872	29.52	460	463	0.61	0.842	7.4	55.6
10X-4, 101–121	135.95	27.0	1.33949	7.58	6.117	556.1	1.2	BD	0.27	0.836	27.41	461	477	3.25	0.830	7.9	50.2
11X-1, 80–90	141.00	22.0	—	7.41	5.631	549.2	0.6	0.09	0.27	0.850	27.77	478	469	1.95	0.871	10.2	49.2
Bottom water					2.04	543				0.836	28.08	466			0.859	10.15	52.5

Notes: * = value was determined colorimetrically aboard ship, † = value was determined postcruise via ICP-OES. Volumes are crude approximates only. Na_{charge} is the Na value that we calculate from charge balance based on Cl, Br, sulfate, alkalinity, Mg, K, and Ca balance. Bottom water values were calculated based on the chlorinity of samples from the uppermost ~1 mbsf from Sites C0014, C0015, and C0017 (n = 4) and assuming that the elements are in constant proportion to chloride; we also make the assumption that chlorinity and chloride are the same. BD = below detection limit, — = no data.

Table T6 (continued).

Core, section, Interval (cm)	Depth (mbsf)	Ca (mM)	Zn (µM)	Rb (µM)	Mo (nM)	Cs (nM)	U (nM)	Boron (µM)	Ba (µM)	Fe (µM)	Li (µM)	Mn (µM)	Si (µM)†	Sr (µM)
331-C0017A-														
1H-1, 80–90	0.80	10.37	0.688	1.73	127	3.4	1.8	522	0.46	3.6	40.0	11.6	0.56	82.1
1H-5, 88–98	6.52	10.39	0.345	1.61	106	4.2	3.9	527	0.51	1.0	37.1	28.4	0.56	86.8
331-C0017B-														
1H-2, 85–95	11.06	10.01	0.419	1.48	76	4.0	1.4	509	0.54	7.1	38.0	16.7	0.72	87.5
1H-5, 70–80	15.14	10.31	0.182	1.37	66	6.1	3.0	511	0.55	2.7	38.0	12.2	0.63	86.9
331-C0017C-														
1H-2, 60–70	20.31	10.76	0.477	1.74	221	4.5	3.3	430	0.51	44.3	37.6	19.5	0.53	88.8
1H-5, 115–125	25.09	10.96	0.690	1.71	101	4.7	6.4	448	0.42	6.7	43.2	12.7	0.40	86.7
2H-1, 65–75	28.45	10.60	0.170	1.59	2316	8.5	19.7	401	0.54	0.6	41.4	3.1	0.19	87.2
2H-2, 65–75	29.85	10.44	0.255	1.84	155	5.6	12.7	446	0.35	0.7	47.3	0.5	0.18	90.9
331-C0017D-														
1H-3, 80–90	63.62	10.96	0.276	1.54	430	6.7	4.1	378	0.78	1.0	41.4	6.2	0.73	86.9
1H-5. 80–90	66.44	11.00	0.534	1.51	1098	6.4	4.6	398	0.68	0.8	39.2	6.5	0.71	88.0
1H-6, 110–120	68.15	10.87	0.253	1.46	111	8.3	4.1	355	0.76	0.8	39.5	5.0	0.76	86.4
2H-5, 30–40	75.15	11.23	0.847	1.18	217	6.5	16.7	323	0.74	0.7	40.1	6.5	0.88	87.9
6X-1, 66–76	94.86	15.25	0.523	0.81	160	11.7	0.9	218	1.26	0.5	54.9	12.7	0.39	96.6
7H-2, 112–122	106.23	14.91	0.281	0.85	234	2.7	3.8	231	0.93	0.6	59.1	14.8	0.40	100.0
7H-4, 42–52	108.34	15.30	0.411	0.67	213	1.6	1.8	205	1.21	0.6	55.6	18.0	0.36	98.5
7H-5, 80–90	110.14	14.22	0.385	0.99	191	3.6	1.6	270	1.19	1.0	51.8	16.9	0.55	97.6
9X-5, 25–35	126.13	18.13	0.405	0.84	167	2.2	2.5	201	1.48	0.9	61.2	15.6	0.29	114.2
9X-8, 75–90	130.86	16.72	0.483	0.84	370	4.1	2.1	158	1.55	0.6	57.2	16.5	0.26	109.7
10X-1, 88–102	131.58	14.73	0.496	1.00	351	4.9	5.0	136	2.05	0.6	46.3	17.4	0.75	98.9
10X-4, 101–121	135.95	16.28	0.666	1.24	223	4.2	2.6	148	1.44	0.8	58.2	34.8	0.26	98.6
11X-1, 80–90	141.00	16.67	2.070	2.15	203	9.3	3.5	204	2.17	0.6	63.9	47.5	0.25	97.2
Bottom water		10.23						410			26.2			90.6

Table T7. Concentrations of hydrocarbons observed in safety gas vials, Site C0017.

Core, section, interval (cm)	Depth (mbsf)	CH_4 in headspace (ppm)	C_2H_6 in headspace (ppm)	C_3H_8 in headspace (ppm)	Butane, ethylene, and/or propylene (Y or N)	Sediment mass (g)	CH_4 in pore water (μM)
331-C0017A-							
1H-1, 136–140	1.36	2.16	BD	BD	N	7.295	0.4
331-C0017B-							
1H-1, 136.5–140.5	10.17	2.42	BD	BD	N	4.692	0.4
331-C0017C-							
1H-1, 137–141	19.67	2.48	BD	BD	N	5.571	0.2
2H-1, 136–140	29.16	2.10	BD	BD	N	6.921	0.4
331-C0017D-							
1H-1, 137–141	61.37	1.15	BD	BD	N	2.285	1.0
2H-1, 137–141	70.57	2.22	BD	BD	N	3.331	0.6
6X-1, 124–128	95.44	2.80	BD	BD	N	6.788	0.2
7H-2, 137–141	106.48	2.76	BD	BD	N	5.099	0.2
8T-CC, 5–9	112.25	3.84	BD	BD	N	0.693	3.4
9X-3, 0–4	123.13	2.12	BD	BD	N	6.121	0.2
10X-2, 137–141	133.49	15.45	BD	BD	N	3.703	2.2
11X-1, 136.5–140.5	141.57	16.01	BD	BD	N	6.208	1.3

BD = below detection.

Table T8. Concentrations of H_2 and CH_4 in science gas, Site C0017.

Hole, core, section, interval (cm)	Depth (mbsf)	H_2 in headspace (ppm)	CH_4 in headspace (ppm)	Sample mass (g)	H_2 in pore water (nM)	CH_4 in pore water (μM)
331-						
C0017A-1H-1, 136–140	1.36	BD	BD	6.4	BD	BD
C0017A-1H-3, 137–141	4.18	BD	BD	5.3	BD	BD
C0017B-1H-1, 136.5–140.5	10.17	BD	BD	4.3	BD	BD
C0017B-1H-3, 137–141	13.00	1.7	BD	5.3	227.2	BD
C0017B-1H-5, 138–142	15.82	BD	BD	7.3	BD	BD
C0017C-1H-1, 137–141	19.67	BD	BD	3.2	BD	BD
C0017C-1H-4, 137–141	23.90	26.7	BD	6.3	4186.1	BD
C0017D-2H-1, 137–141	27.80	BD	BD	4.7	BD	BD
C0017C-2H-4, 136.5–140.5	32.55	BD	BD	3.7	BD	BD
C0017D-1H-1, 137–141	61.34	BD	1.3	6.4	BD	0.2
C0017D-1H-3, 137–141	64.09	BD	BD	2.6	BD	BD
C0017D-1H-5, 137–141	66.84	2.9	BD	4.2	477.8	BD
C0017D-2H-1, 137–141	70.55	BD	BD	3.5	BD	BD
C0017D-2H-3, 137–141	73.34	2.4	BD	2.1	769.2	BD
C0017D-2H-4, 137–141	74.74	BD	BD	3.7	BD	BD
C0017D-6X-1, 124–128	95.44	BD	BD	6.1	BD	BD
C0017D-7H-2, 137–141	106.34	BD	BD	3.9	BD	BD
C0017D-7H-4, 137.5–141.5	109.01	BD	BD	6.5	BD	BD
C0017D-7H-5, 137.5–141.5	110.35	BD	BD	4.7	BD	BD
C0017D-8T-CC, 5–9	112.25	BD	BD	0.3	BD	BD
C0017D-9X-3, 0–4	122.99	BD	BD	3.9	BD	BD
C0017D-9X-4, 137–141	125.44	BD	BD	4.4	BD	BD
C0017D-9X-6, 137–141	127.98	BD	BD	4.0	BD	BD
C0017D-10X-2, 137–141	133.49	2.9	4.6	4.0	1184.7	1.9
C0017D-11X-1, 136.5–140.5	141.57	BD	7.6	6.2	BD	1.4
C0017D-11X-2, 136.5–140.5	142.97	1.3	4.7	5.3	328.7	1.2

BD = below detection.

Table T9. Carbon, nitrogen, and sulfur, Site C0017.

Core, section, interval (cm)	Depth (mbsf)	IC (wt%)	$CaCO_3$ (wt%)	TN (wt%)	TC (wt%)	TS (wt%)	TOC (wt%)	TOC/TN	TOC/TS
331-C0017A-									
1H-1, 35.5–37.5	0.36	1.681	14.004	0.096	2.505	0.471	0.824	8.626	1.752
1H-2, 76.5–78.5	2.17	2.240	18.662	0.083	2.957	0.252	0.718	8.630	2.853
1H-3, 54–56	3.35	0.928	7.735	0.019	1.082	0.096	0.154	8.269	1.609
1H-4, 122–124	5.44	5.372	44.766	BD	5.547	0.035	0.175	NA	4.987
1H-5, 115–117	6.79	2.092	17.435	0.099	2.996	0.200	0.904	9.091	4.519
1H-6, 62–64	7.66	1.860	15.501	0.105	2.817	0.257	0.957	9.070	3.717
331-C0017B-									
1H-1, 103–105	9.83	2.380	19.828	0.076	3.012	0.099	0.632	8.326	109.642
1H-3, 80–82	12.43	1.612	13.434	0.091	2.399	0.273	0.787	8.604	94.079
1H-4, 80–82	13.84	1.777	14.808	0.097	2.662	0.148	0.885	9.100	93.524
1H-5, 80–82	15.24	2.018	16.819	0.093	2.807	0.332	0.789	8.513	91.843
1H-6, 57–59	16.43	1.114	9.280	0.020	1.279	0.244	0.165	8.128	399.191
1H-7, 80–82	18.07	1.686	14.052	0.086	2.424	0.236	0.737	8.525	98.569
331-C0017C-									
1H-1, 114–116	19.44	1.288	10.735	0.033	1.570	0.102	0.281	8.611	2.772
1H-2, 118–120	20.89	3.082	25.682	0.067	3.634	0.071	0.552	8.272	7.729
1H-3, 70–72	21.82	1.669	13.909	0.081	2.343	0.166	0.674	8.357	4.047
1H-4, 64–66	23.17	0.706	5.883	0.016	0.840	0.126	0.134	8.162	1.061
1H-5, 60–62	24.54	2.955	24.622	0.073	3.611	0.115	0.656	8.931	5.701
1H-6, 97–99	26.32	3.846	32.052	0.034	3.972	0.032	0.125	3.720	3.948
1H-7, 73–75	27.49	0.058	0.486	0.007	0.083	0.081	0.024	3.397	0.304
2H-1, 90–92	28.70	0.031	0.255	0.006	0.054	0.098	0.024	3.954	0.244
2H-2, 97–99	30.17	5.070	42.247	0.025	5.165	0.049	0.096	3.790	1.934
2H-3, 30–32	30.58	0.049	0.410	0.007	0.076	0.119	0.027	4.015	0.224
2H-4, 84–86	31.93	0.004	0.031	BD	0.011	0.060	0.007	NA	0.119
2H-5, 50–52	32.99	0.002	0.013	BD	0.011	0.067	0.010	NA	0.143
2H-6, 60–62	34.50	0.002	0.013	BD	0.008	0.089	0.007	NA	0.077
2H-7, 45–47	35.76	0.004	0.030	BD	0.012	0.068	0.008	NA	0.118
331-C0017D-									
1H-1, 131–133	61.31	0.021	0.175	BD	0.037	0.096	0.016	NA	0.162
1H-2, 99–101	62.40	0.002	0.013	0.006	0.023	0.057	0.022	3.389	0.379
1H-3, 121–123	64.03	0.001	0.012	0.010	0.033	0.038	0.031	3.113	0.834
1H-4, 29–31	64.52	0.000	0.000	0.010	0.035	0.029	0.035	3.382	1.210
1H-5, 48–50	66.12	0.000	0.000	0.011	0.035	0.044	0.035	3.168	0.802
1H-6, 26–28	67.31	0.002	0.014	0.013	0.045	0.040	0.043	3.294	1.071
1H-7, 30–32	68.76	0.007	0.058	0.006	0.037	0.029	0.030	4.779	1.051
2H-1, 120–122	70.40	0.029	0.239	BD	0.049	0.084	0.020	NA	0.236
2H-2, 112–114	71.73	0.001	0.008	0.041	0.101	0.049	0.100	2.459	2.046
2H-3, 52–54	72.55	0.002	0.013	0.042	0.159	0.031	0.158	3.739	5.055
2H-4, 51.5–53.5	73.95	0.000	0.003	BD	0.012	0.120	0.012	NA	0.099
2H-5, 65.5–67.5	75.50	0.001	0.007	BD	0.016	0.053	0.015	NA	0.287
2H-6, 62–64	76.87	0.024	0.199	0.087	0.770	0.136	0.746	8.613	5.479
2H-7, 81.5–83.5	78.48	0.001	0.005	BD	0.024	0.073	0.023	NA	0.320
6X-1, 63–65	94.83	0.776	6.466	0.043	1.155	0.248	0.379	8.809	1.531
6X-2, 16–18	95.64	0.877	7.308	0.051	1.323	0.377	0.446	8.805	1.184
7H-2, 30–32	105.41	0.814	6.781	0.061	1.355	0.182	0.541	8.879	2.978
7H-3, 134–136	107.86	0.599	4.991	0.022	0.787	0.112	0.188	8.504	1.681
7H-4, 110–112	109.02	0.553	4.606	0.061	1.075	0.468	0.522	8.608	1.116
7H-5, 42–44	109.76	0.083	0.695	0.008	0.162	0.713	0.078	9.918	0.110
7H-6, 66–68	111.41	0.706	5.881	0.018	0.728	0.430	0.023	1.256	0.053
8T-CC, 0–2	112.20	0.699	5.826	0.043	1.077	0.430	0.378	8.756	0.879
7H-CC, 22–24	112.43	0.001	0.011	BD	0.019	0.014	0.017	NA	1.257
9X-2, 110–112	122.91	0.913	7.611	0.046	1.273	0.468	0.360	7.798	0.769
9X-4, 100–102	125.47	0.915	7.627	0.049	1.312	0.545	0.397	8.091	0.729
9X-6, 100–102	128.29	0.879	7.326	0.044	1.239	0.276	0.360	8.135	1.304
9X-8, 70–72	130.81	0.956	7.968	0.051	1.368	0.247	0.412	8.012	1.669
10X-2, 60–62	132.72	0.525	4.373	0.021	0.738	0.224	0.213	10.009	0.951
10X-4, 32–34	135.26	1.166	9.720	0.049	1.625	0.115	0.459	9.277	3.991
10X-CC, 40–42	137.12	1.045	8.704	0.058	1.512	0.179	0.467	8.027	2.614
11X-1, 70–72	140.90	1.219	10.159	0.019	1.474	0.035	0.255	13.603	7.271
11X-2, 68–70	142.29	0.482	4.017	0.047	0.895	0.106	0.413	8.702	3.893
11X-3, 75–77	143.76	0.002	0.014	0.046	0.302	0.048	0.300	6.488	6.239
11X-CC, 33–35	144.67	BD	BD	0.007	0.038	0.078	0.038	5.139	0.490

Notes: IC = inorganic carbon, TN = total nitrogen, TC = total carbon, TS = total sulfur, TOC = total organic carbon. BD = below detection. NA = not applicable.

Table T10. Results of direct cell counting, Site C0017.

Core, section	Depth (mbsf)	Cells/mL sediment
331-C0017A-		
1H-1	0.65	2.35E+07
1H-5	6.37	3.22E+07
331-C0017B-		
1H-2	10.811	2.39E+07
1H-5	14.802	9.51E+05
331-C0017C-		
1H-2	20.088	4.42E+06
1H-5	24.632	8.42E+06
1H-7	26.579	1.45E+06
2H-1	28.35	2.52E+06
2H-2	29.95	2.52E+06
331-C0017D-		
1H-3	63.633	7.51E+05
1H-5	66.382	5.81E+05
1H-6	68.052	ND
1H-6	68.262	ND
6X-1	94.96	ND
7H-4	108.197	ND
9X-8	130.1	ND
10X-4	136.145	ND
11X-1	141.1	ND

ND = not detected.

Table T11. Results of contamination tests using fluorescent microspheres, Site C0017.

Core, section	Depth (mbsf)	Spheres/mL sediment	
		Interior	Outer edge
331-C0017A-			
1H-1	0.65	ND	1.28E+03
1H-5	6.37	ND	2.91E+03
331-C0017B-			
1H-2	10.811	ND	2.45E+04
1H-5	14.802	ND	2.32E+02
331-C0017C-			
1H-2	20.088	ND	6.99E+04
1H-5	24.632	ND	3.05E+03
1H-7	26.579	ND	ND
2H-1	28.35	ND	9.59E+03
2H-2	29.95	ND	1.45E+02
331-C0017D-			
1H-3	63.633	ND	ND
1H-5	66.382	ND	ND
1H-6	68.052	ND	ND
2H-5	74.873	ND	5.08E+03
7H-4	108.197	ND	6.97E+03

ND = not detected.

Table T12. Results of contamination tests using fluorescent microspheres, Site C0017.

Core, section	Depth (mbsf)	PFT in test vial gas phase (ppm)		Sample weight in test vial (g)		PFT per g sample (ppm)	
		Interior	Outer edge	Interior	Outer edge	Interior	Outer edge
331-C0017A-							
1H-1	0.65	ND	5.16E–02	1.17	3.38	ND	1.53E–02
1H-5	6.37	ND	4.52E–02	2.47	0.91	ND	4.97E–02
331-C0017B-							
1H-2	10.811	ND	1.61E–01	2.17	1.95	ND	8.26E–02
1H-5	14.802	ND	5.99E–02	3.83	1.78	ND	3.37E–02
331-C0017C-							
1H-2	20.088	ND	4.93E–02	5.21	1.97	ND	2.50E–02
1H-7	26.579	ND	1.71E–03	0.78	1.43	ND	1.20E–03
2H-2	29.95	ND	1.21E–02	4.95	3.08	ND	3.93E–03
331-C0017D-							
1H-3	63.633	2.30E–03	2.03E–02	1.17	2.73	1.97E–03	7.44E–03
1H-5	66.382	5.94E–03	3.23E–03	2.25	2.93	2.64E–03	1.10E–03
1H-6	68.052	ND	4.41E–03	2.56	0.53	ND	8.32E–03
2H-5	74.873	ND	8.23E–03	2.81	3.89	ND	2.12E–03
6X-1	94.96	ND	4.12E–03	3.54	2.22	ND	1.86E–03
7H-4	108.197	3.94E–03	5.99E–03	2.41	4.06	1.63E–03	1.48E–03
9X-8	130.1	6.56E–03	1.37E–02	3.29	4.60	1.99E–03	2.98E–03
10X-4	136.1	3.36E–03	NT	3.77	NT	8.91E–04	NT
11X-1	141.1	2.19E–02	4.93E–02	4.66	2.92	4.70E–03	1.69E–02

PFT = perfluorocarbon tracer. ND = not detected, NT = not tested.

Table T13. Cultivation experiment results for putative iron oxidizers, Site C0017.

Depth (mbsf)		Hole, core, section, interval (cm)	Growth media	
Top	Bottom		ASW A	ASW B
		331-		
0.65	0.80	C0017A-1H-1, 65–80	—	ND
20.09	20.23	C0017C-1H-2, 45–60	+	+
24.63	24.82	C0017C-1H-5, 95–115	—	ND
26.26	26.28	C0017C-1H-6, 119–121	+++	—
26.57	26.76	C0017C-1H-7, 15–35	++	—
26.57	26.76	C0017C-1H-7, 15–35	+++	—
28.35	28.45	C0017C-2H-1, 55–65	+++	++
29.95	30.15	C0017C-2H-2, 75–95	—	—

+++ = good growth (lots of cells), ++ = medium growth, + = little growth (a few cells), — = no growth. ND = no data.

Table T14. Average porosity, bulk density, grain density, thermal conductivity, and formation factor, Site C0017.

Hole	Porosity (%)	Bulk density (g/cm^3)	Grain density (g/cm^3)	Thermal conductivity (W/[m·K])	Formation factor
331-					
C0017A	0.65 ± 0.07	1.57 ± 0.09	2.60 ± 0.06	0.94 ± 0.09	3.94 ± 1.22
C0017B	0.63 ± 0.05	1.60 ± 0.04	2.61 ± 0.15	1.07 ± 0.06	3.77 ± 0.40
C0017C	0.65 ± 0.14	1.56 ± 0.23	2.54 ± 0.25	0.83 ± 0.27	4.57 ± 2.11
C0017D	0.52 ± 0.13	1.81 ± 0.25	2.62 ± 0.21	1.23 ± 0.32	6.52 ± 1.68
Average:	0.57 ± 0.13	1.71 ± 0.25	2.60 ± 0.20	1.09 ± 0.30	5.41 ± 1.98

Error is the standard deviation of the average.

Table T15. APCT3 temperature measurements, Site C0017.

Hole, core	Unit	Depth CSF (m)	Equilibrium temperature (°C)	Bottom water temperature (°C)
331-				
C0017B-1H	I	18.3	5.24	4.89
C0017C-2H		37.3	5.97	5.23
C0017D-1H	II	69.2	25.08	4.38
C0017D-2H		78.7	35.18	4.48
C0017D-3H		84.7	39.4	4.57
C0017D-4H		84.7	—	5.40
C0017D-7H	III	112.2	44.12	5.75
C0017D-12H*		150.7	90	4.24

— = no temperature calculated. * = temperature from thermoseal strips.

Table T16. Measured values for the thermal gradient, thermal conductivity, and estimated heat flow, Site C0017.

Unit	Thermal gradient (K/m)	Thermal conductivity (W/[m·K])	Heat flow
I	0.03	0.95	0.0285
II	0.43	0.82	0.3526
III	0.89	1.37	1.2193